Efficient characterization of multiple binding sites of small molecule imaging ligands on amyloid-beta, 4-repeat/full-length tau and alpha-synuclein

Jens Sobek,[1*] Junhao Li,[2] Benjamin F. Combes,[3] Juan A Gerez,[4] Peter K. Nilsson,[5] Martin T. Henrich,[6] Fanni F. Geibl,[6] Kuangyu Shi[7], Axel Rominger[7], Wolfgang H. Oertel,[6] Roger M. Nitsch,[3] Agneta Nordberg,[8] Hans Ågren,[2] Roland Riek,[4] Ruiqing Ni,[3,9]*

[1]Functional Genomics Center, University of Zurich & ETH Zurich, Zurich, Switzerland

[2]Institute for Regenerative Medicine, University of Zurich, Zurich, Switzerland

[3]Department of Physics and Astronomy, Uppsala University, Uppsala, Sweden

[4]Laboratory of Physical Chemistry, Department of Chemistry and Applied Biosciences, ETH Zurich, Switzerland

[5]Division of Chemistry, Department of Physics, Chemistry and Biology, Linköping University, Linköping, Sweden

[6]Department of Psychiatry and Psychotherapy, Philipps-University Marburg; Department of Neurology, Philipps-University Marburg, Marburg, Germany

[7]Department of Nuclear Medicine, Inselspital, Bern University Hospital, University of Bern, Freiburgstr. 18, 3010, Bern, Switzerland.

[8]Division of Clinical Geriatrics, Center for Alzheimer Research, Department of Neurobiology, Care Sciences and Society, Karolinska Institutet, Stockholm, Sweden

[9]Institute for Biomedical Engineering, University of Zurich & ETH Zurich, Zurich, Switzerland

Corresponding author: Dr. Ruiqing Ni

Email: ruiqing.ni@uzh.ch;Phone: +41 44 634 88 86

Address: Wagistrasse 12, 8952 Zurich, Switzerland

Abstract

Aim: There is an unmet need for compounds that detect alpha-synuclein (αSyn) and 4-repeat tau, which are critical in many neurodegenerative diseases for diagnostic and therapeutic purposes. Here, we aim to develop an efficient surface plasmon resonance (SPR)-based method to facilitate the characterization of small molecule ligands/compounds to these fibrils.

Methods: SPR measurements were conducted to characterize the binding properties of fluorescent ligands/compounds towards recombinant $A\beta_{42}$, K18 4-repeat/full-length tau and αSyn fibrils. In silico modelling was performed to examine the binding pockets of ligands on αSyn fibrils. Immunofluorescence staining with fluorescence ligands and specific antibodies on postmortem brain tissue slices from patients with Parkinson's disease and disease mouse models was performed.

Results: We optimized the protocol for immobilizing $A\beta_{42}$, K18 tau, full-length tau and αSyn fibrils in a controlled aggregation state on SPR sensor chips. The results from the analysis of binding kinetics suggested the presence of at least two binding sites for all fibrils, including luminescent conjugated oligothiophenes (HS-169, HS-84, h-FTAA and q-FTAA), pyridine derivative PBB5, nonfluorescent methylene blue and lansoprazole. In silico modelling studies for αSyn (6H6B) showed four binding sites with preference to S4. Immunofluorescence staining validated the detection of pS129-positive αSyn in brain tissue from Parkinson's disease patients, αSyn PFF-injected mice, 6E10-positive Aβ in arcAβ mice, and AT-8/AT-100-positive in tau pR5 tau mice, respectively.

Conclusions: SPR measurements of ligands and small molecules binding to $A\beta_{42}$, 4R and full-length tau and αSyn fibrils suggest the existence of multiple binding sites. This approach

may provide efficient characterization of compound binding properties towards these fibrils important in neurodegenerative diseases.

Keywords: alpha-synuclein, amyloid-beta, binding sites, in silico, kinetics, ligand, surface plasmon resonance, tau

1 Introduction

Neurodegenerative diseases represent a tremendous unmet clinical need. A common feature of these diseases is the abnormal cerebral accumulation and spreading of pathological protein aggregates, affecting selective vulnerable circuits in a disease-specific pattern (Jucker and Walker, 2018; Riek and Eisenberg, 2016). Alzheimer's disease (AD) is pathologically hallmarked by amyloid-β (Aβ) plaques and neurofibrillary tangles of hyperphosphorylated tau. Other tauopathies include frontotemporal dementia with 4R and 3R tau, progressive supranuclear palsy (PSP) with 4R tau, and corticobasal degeneration (CBD) with 3R tau accumulation (Spillantini and Goedert, 2013). α-synucleinopathy is characterized by the accumulation of alpha-synuclein (αSyn) in Parkinson's disease (PD), dementia with Lewy bodies and multiple system atrophy (MSA). The use of positron emission tomography (PET) with Aβ and tau imaging ligands has facilitated the early/differential diagnosis of AD (Dubois et al., 2021). Currently, there is an unmet clinical need for PET ligands for 4-repeat tau and αSyn aggregates to assist in diagnostic and clinical outcome evaluations. Several imaging ligands are currently in the pipeline, such as [^{18}F]ACI-12589 (Smith et al., 2022), [^{11}C]MODAG-001 (Kuebler et al., 2021), [^{18}F]SPAL-T-06 (Matsuoka et al., 2022) and [^{18}F]UCB-2897 (NCT05274568). In addition, optical imaging ligands have been developed and applied in mechanistic and treatment studies using disease animal models recapitulating amyloidosis/tauopathy/αSyn. Using two-photon and diffuse optical imaging approaches, several imaging ligands, such as BTA-1, methoxy-X04, BF-158, PBB5, luminescent conjugated oligothiophenes (LCOs), BODIPY derivatives and fluorescently labelled antibodies, have been reported (Bian et al., 2021; Calvo-Rodriguez et al., 2019a; Hou et al., 2023; Krishnaswamy et al., 2014; Kuchibhotla et al., 2014; McMurray et al., 2021; Ni et al., 2020; Reyes et al., 2021; Tanriöver et al., 2020; Torre-Muruzabal et al., 2023; Vagenknecht et al., 2022; Verwilst et al., 2017; Wu et al., 2018). A number of experimental techniques,

including fluorescence assays, radioligand competition assays (LeVine, 2005; Malarte et al., 2020; Ni et al., 2017; Ni et al., 2013a; Ni et al., 2018; Ni et al., 2013b; Ni et al., 2021a; Yap et al., 2021), nuclear magnetic resonance spectroscopy (Gerez et al., 2020; Schütz et al., 2018), and cryogenic electron microscopy (cryo-EM) (Antonschmidt et al., 2022; Shi et al., 2021a), have been reported to investigate interactions between ligands and Aβ peptides (Ferrie et al., 2020; Sanna et al., 2021; Shi et al., 2021b; Shimogawa and Petersson, 2021; Yang et al., 2022) and have demonstrated multiple ligand binding sites. *In silico* studies have also often been applied to study the interactions between ligands and proteinopathies/fibrils (Kuang et al., 2020; Kuang et al., 2019; Murugan et al., 2016; Murugan et al., 2018; Zhou et al., 2021).

Surface Plasmon Resonance (SPR) is the method of choice to study the kinetics of interactions for a wide range of molecular systems and has been widely used in pharmaceutical, biosensing, and biomolecular research (Erbaş and Inci, 2022; Karlsson, 2004). The SPR approach has been more commonly used in detecting Aβ and tau monomers in biological samples, such as blood or cerebrospinal fluid, as diagnostic biomarkers (Kim et al., 2016; Nangare and Patil, 2021; Rezabakhsh et al., 2020; Stravalaci et al., 2012). It has also been used to investigate Aβ elongation, aggregation dynamics (Ryu et al., 2008; Stravalaci et al., 2011) and interactions with aggregation inhibitors (De Simone et al., 2013; Dehghani et al., 2021; Frenzel et al., 2014; Marasco et al., 2021). A few studies have reported SPR for αSyn fibrils (Honarmand et al., 2019; Jha et al., 2017; Sangwan et al., 2020; Thom et al., 2021; Yin et al., 2020), tau fibrils (Haghaei et al., 2020; Lisi et al., 2017; Rojo et al., 2010), and Aβ fibrils (Martins et al., 2015; Rojo et al., 2010) for characterization of interactions with resveratrol and lansoprazole. However, binding kinetics and binding site determination need further optimization of the experimental protocol and modelling.

Here, we established a SPR pipeline to determine the binding kinetics of small molecules (imaging ligands and nonfluoresence compounds) on $A\beta_{42}$, K18 tau, full-length tau and αSyn fibrils. We further examined the binding sites of fluorescence ligands on αSyn fibrils by *in silico* modelling and immunofluorescence staining in postmortem human brain tissues from patients with PD and from PFF-injected mouse models.

2 Methods

2.1 Chemicals and antibodies

Luminescent conjugated oligothiophenes (LCOs), including HS-84, HS-169, h-FTAA, and q-FTAA, were synthesized and provided by KPRN (Linköping, Sweden) (Klingstedt et al., 2011; Shirani et al., 2015). Methylene blue (Sigma Aldrich, Switzerland), lansoprazole (Sigma Aldrich, Switzerland), and pyridine-derivative PBB5 (RadiantDye, Germany) were purchased from the indicated sources (chemical structures in **SFig. 1**). Detailed information on the chemicals and antibodies used in the study is provided in **STable 1**.

2.2 Recombinant $A\beta_{42}$, K18 tau, full-length tau and αSyn fibril production, characterization and detection by fluorescence ligands.

Recombinant $A\beta_{42}$, K18 tau (4-repeat), full-length tau and αSyn were expressed and produced by *E. coli* as described previously (detailed methods in supplementary material) (Burmann et al., 2019; Gerez et al., 2019). As a substrate for HRP, Pierce ECL and Western Blotting Substrate (Thermo Fisher Scientific, U.S.A.) were used to detect $A\beta_{42}$, and αSyn. To detect K18 tau, ECL Prime Western Blotting Detection reagents (Cytiva, U.S. A.) were used. Images of the resulting blots were taken with an ImageQuant LAS 4000 (GE Healthcare). After incubation of the protein solutions, fibrillization was verified by thioflavin T

fluorescence assay: 45 µL of thioflavin T (5 µM, Sigma Aldrich, U.S.A.) was mixed with either 2 µL of the incubated αSyn, 5 µL of K18 tau, or 5 µL of $A\beta_{42}$ in a 45 µL quartz cuvette (quartz SUPRASIL Ultra Micro Cell, Hellma). Mass photometry was used to measure the mass of the fibrils at FGCZ, ETH Zurich.

Transmission electron microscopy (TEM) was performed by adding 4 µL of the fibril samples (~50 µM) in PBS directly to the negatively glow-discharged carbon-coated copper grids, followed by incubation for 1 minute at room temperature. The excess solution was gently removed using Whatman filter paper. Samples were stained with 10 µL of an aqueous phosphotungstic acid solution (1%, pH 7.2) for 1 minute. The excess stain on the grid was then wiped off with filter paper, washed with double-distilled water and air dried. Finally, the images were recorded on a Morgagni 268 electron microscope (FEI GmbH, Germany) at ScopeM, ETH Zurich.

For fluorescence assays with different fluorescence-emitting ligands, mixtures of different fibrils and ligands were incubated for 1 minute and resuspended in a pipette, and the fluorescence intensity over a wide range of spectra was measured with a spectrofluorometer (FluoroMax-4, Horiba Jobin Yvon) using a known excitation wavelength for these ligands.

2.3 Surface Plasmon Resonance

SPR measurements were conducted in HBS buffer at 20 °C using Biacore instruments T200 and S200 (Cytiva, Uppsala, Sweden). $A\beta_{42}$, tau, and αSyn recombinant fibrils were immobilized in the flow cell of sensor chips produced by Xantec (Düsseldorf, Germany) and Cytiva by coupling fibril amine groups to sulfo-N-hydroxysuccinimide (sulfo-NHS)-activated carboxylic acid groups on the chip surface. Since no nonbinding fibril(s) were available, the

reference flow cell remained empty. Different chip surfaces were tested to obtain a high immobilization density and low nonspecific adsorption of analytes, including carboxymethylated dextran surface CM5 (Cytiva, Sweden), carboxymethyldextran hydrogel surface CMD200M, linear polycarboxylate hydrogel surface HC30M and HC1500M, linear polycarboxylate hydrogel (reduced charge) surface HLC30M, and zwitterionic hydrogel surface ZC150D (all from Xantec, Germany). All steps for surface preparation and immobilization were conducted at a flow rate of 5 µL/min. Surface carboxylic acid groups were activated with 0.2 M sulfo-NHS and 1-ethyl-3-(3-dimethylaminopropyl)carbodiimide (EDC) (both from Xantec) 0.1 M (CM5 and CMD200M: 0.05 M) in 10 mM 2-(N-morpholino)ethanesulfonic acid (MES buffer, abcr Swiss AG, Switzerland) at pH 5.0 for 550 s (CM5 and CMD200M: 180 s) using 5 mM MES pH 6.5 as running buffer. K18 tau and αSyn fibrils were diluted to 2.5-10 µM in 5 mM acetate buffer (Fisher Scientific, Switzerland) at pH 4.5 and coupled for 750 s at a flow rate of 5 µL/min on all surfaces except for ZD150D. Surfaces were blocked with 1 M ethanolamine (Xantec, Germany) for 500 s. On the ZC150D chip, K18 tau, αSyn and $A\beta_{42}$ were immobilized at 2.5 - 10 µM in 5 mM MES pH 6.5 for 750 s to a surface activated with 500 mM EDC and 100 mM sulfo-NHS for 600 s in 5 mM MES pH 6.5. Finally, the surface was blocked with 1 M glycine in 10 mM MES pH 6.5.

Binding kinetics were measured after a stabilization period of a few hours that was necessary due to a slightly decreasing baseline presumably caused by a slow dissociation of fibrils. Immobilized fibrils were stable for a few days. Kinetic constants for binding were determined by injection of a dilution series of 5-8 concentrations of analyte in HBS buffer (Teknova, USA) at a flow rate of 30 µL/min in duplicate ("full kinetics"). Since no regeneration conditions were found that did not lead to decomposition of the fibrils, single cycle kinetics

(Karlsson et al., 2006) were measured in cases of slow dissociation by consecutive injection of 5 analyte concentrations followed by a dissociation period of 10 min.

Data were evaluated using BiaEvaluate v2.03 software (Cytiva, Sweden). Binding kinetics were analysed globally using different kinetic models, including 1+1, a sum of 2 exponentials model ("heterogeneous ligand" in terms of BiaEvaluate), and a sum of three exponentials model that was created using the script editor of the software. The software does not allow the creation of higher-order kinetic models.

2.4 In silico modelling and calculations

The αSyn fibrils were adopted from previous studies (PDB codes: 6H6B (Guerrero-Ferreira et al., 2018; Kumari et al., 2021) and 2N0A (Kuang et al., 2019)). The protein preparation wizard module in the Schrödinger suite (V. 2021-3, Schrödinger LLC, New York, U.S.A.) was used to add hydrogen atoms and determine the protonation states of the ionizable residues. The initial structures of the tested compounds were drawn in the Maestro interface and optimized using the Ligprep module (Schrödinger Release 2021-3: LigPrep, Schrödinger, LLC, New York, U.S.A.). The Glide module was used for docking, in which we used normal inner and outer box sizes of 10 and 20 Å, respectively (Friesner et al., 2004; Halgren et al., 2004). The standard precision (SP) mode was used for dockings, while other settings were left as default in Glide. The top 1 scored binding pose of each ligand–αSyn complex was subjected to molecular dynamics (MD) simulations. All MD simulations were carried out for 100-ns production with the OPLS-4 force field (Lu et al., 2021) using the Desmond module. In each simulation, the protein□ligand complex was centered into an orthorhombic box with a boundary buffer of 12 Å, and ~24 000 TIP3P water (Jorgensen et al., 1983) molecules and counter ions were added to neutralize the system. Additional Na^+ and Cl^- were added to reach

a 0.15 M salt concentration. Before the production simulations, the system is energy minimized and equilibrated with a Nose□Hoover chain thermostat (300.0 K) (Martyna et al., 1992) and Martyna-Bobias-Klein barostat (1.0 atm) (Martyna et al., 1994) using the default protocol implemented in Desmond. Molecular mechanics (MM)/generalized born solvent accessibility (GBSA)) (Kollman et al., 2000) binding free energy for each ligands was averaged from a total of 200 snapshots evenly extracted from the 100-ns trajectories. The Prime module [Schrödinger Release 2021-3: Prime, Schrödinger, LLC, New York, NY, 2021.] was used for the MM/GBSA calculations. The protein□ligand complexes were refined and optimized using the OPLS4 force field with the VSGB (variable dielectric surface generalized Born) continuum solvation model (Li et al., 2011). For the minimization, the residues within 5 Å of the ligand were included. After that, the MM/GBSA method implemented in the Prime module was used to rescore the binding poses. Root-mean-square deviation (RMSD) analysis of the average distance between a group of atoms (e.g., backbone atoms of the four binding sites on αSyn) was performed.

2.5 Postmortem human brain tissue

Three PD cases (mean age 72.3[9.5]) each with a clinical diagnosis confirmed by pathological examination of Lewy bodies (Braak LB 6, with tau Braak 0-1 and Aβ O), and one nondemented control aged 69 y (Braak LB 0, with tau Braak 1 and Aβ −), were included in this study (detailed information in **Table 1**). Paraffin-embedded autopsy brain tissues from the medulla oblongata and cerebellum with high αSyn inclusion accumulation were obtained from the Netherlands Brain Bank (NBB), Netherlands. All materials had been collected from donors or from whom written informed consent for a brain autopsy and the use of the materials and clinical information for research purposes had been obtained by the NBB. The study was conducted according to the principles of the Declaration of Helsinki and

subsequent revisions. All experiments on autopsied human brain tissue were carried out in accordance with ethical permission obtained from the regional human ethics committee in Canton Zurich and the medical ethics committee of the VU Medical Center for the NBB tissue.

2.6 Animal models

Two transgenic arcAβ mice overexpressing the human APP695 transgene containing the Swedish (K670N/M671L) and Arctic (E693G) mutations under the control of the prion protein promoter and two age-matched nontransgenic littermates of both sexes (18 months of age) (Knobloch et al., 2007; Ni et al., 2021b; Ren et al., 2022). Two transgenic MAPT P301L mice overexpressing human 2N/4R tau under the neuron-specific Thy1.2 promoter (pR5 line, C57B6. Dg background) and two age-matched nontransgenic littermates of both sexes (18 months of age) (Gotz et al., 2001; Massalimova et al., 2021; Vagenknecht et al., 2022). For the αSyn PFF mouse model, two male C57BL/6J mice (Charles River, Sulzfeld, Germany), 8 weeks old at the beginning of the experiment, were used. Animals were housed in individually ventilated cages inside a temperature-controlled room under a 12-hour dark/light cycle with ad libitum access to food and water. For arcAβ and pR5 mice, all experiments were performed in accordance with the Swiss Federal Act on Animal Protection and approved by the Cantonal Veterinary Office Zurich (permit number: ZH162/20). For αSyn PFF mice, procedures performed were in accordance with the ethical standards of the institution at which the studies were conducted (Regierungspräsidium Giessen, GermanyV54–19c2015h01GI20/28). For induction of αSyn pathology in a total volume of 550 nl of αSyn, PFFs with a concentration of 2.5 µg/µl were stereotactically injected in the pedunculopontine nucleus (PPN) as described (Henrich et al., 2020). Twelve weeks postinjection, mice were sacrificed, and tissue was prepared for immunohistochemical

analysis. arcAβ, pR5 and PFF injected mice were perfused under ketamine/xylazine (75/10/2 mg/kg or 50/4.5 mg/kg body weight, *i.p.* bolus injection) with ice-cold 0.1 M phosphate-buffered saline (PBS, pH 7.4) and 4% paraformaldehyde (PFA) in 0.1 M PBS (pH 7.4). After perfusion, the mice were decapitated, and the brains were quickly removed and fixed for 1 or 3 days in 4% PFA (pH 7.4) and 3 days in 30% sucrose solution. Brains were then frozen on dry ice and stored at -80 °C until sectioning.

2.7 *Ex vivo* immunofluorescence and confocal imaging

The details on the antibodies and ligand concentration are described in **STable 1**. Human paraffin-embedded brain sections (3 µm) were deparaffinized and rehydrated prior to an antigen retrieval step (citrate buffer pH 6.0) in a microwave for 20 min at 98 °C. The sections were then costained with anti-αSyn (phospho-S129, pS129) antibody plus fluorescent secondary antibody. Ligands were incubated after secondary antibody for 30 min. Sections were counterstained using 4',6-diamidino-2-phenylindole (DAPI). Mouse brains were embedded in tissue freezing media (OCT Compound, Tissue Tek, USA) and cut into 30-40 µm thick consecutive coronal sections using a cryostat microtome (CM3050 S, Leica, Germany). All sections spanning the complete rostro-caudal extent of the brain were kept in the correct order and stored at 4 °C in cryoprotect-solution (1:1:3 volume ratio of ethylenglycol, glycerol and 0.1 M PBS) until further processing (Henrich et al., 2018). Anti-αSyn pS129 antibodies, anti-phospho-tau antibodies (AT-8, AT-100), or anti-$A\beta_{1-16}$ antibody 6E10, plus fluorescent secondary antibody were used as previously described on brain slices from αSyn PFF-injected mice, arcAβ mice (Ni et al., 2022), and pR5 mice (Vagenknecht et al., 2022). Ligands were incubated after secondary antibody for 30 min. Sections were counterstained using DAPI. The brain sections were imaged at 20× magnification using an Axio Observer Z1 microscope (whole brain slide) and at 63× magnification using a Leica

SP8 confocal microscope (Leica, Germany) for colocalization. Lambda scans were performed using a Leica SP8 confocal microscope for the emission spectrum of the ligands on the staining as previously described to validate the signal (Ni et al., 2020). The images were analysed using Qupath (Bankhead et al., 2017) and ImageJ (NIH, U.S.A).

3 Results

3.1 *In vitro* fluorescence binding assays in recombinant fibrils

We produced $A\beta_{42}$, K18 tau, full-length tau and αSyn fibrils using bacterially produced recombinant monomers. During the processing of K18 tau, full-length tau and αSyn after each step, an aliquot was taken, and at the end, the identity was verified by SDS–PAGE (**SFig. 2**). The monomers were validated using western blotting, and the fibrils were validated using thioflavin T assays and TEM (**Figs. 1-3**). The results from mass photometry indicated that the mass of the resulting fibrils was more than 2 MDa. The fluorescence emission wavelengths of ligands in the presence of fibrils were measured by using fluospectrometer and summarized in **STable. 2**.

3.2 Optimization of the SPR protocol for small molecule ligand binding to Aβ, K18 tau, full-length tau and αSyn fibrils

First, we established and optimized the experimental protocol for SPR measurement of small molecule ligands binding to Aβ, K18 tau, full-length tau and αSyn fibrils. A general problem of SPR measurements of small molecule ligands binding to immobilized fibrils is the large molar mass ratio (small molecule compound: <1000 Da, fibrils >1 MDa), which requires high surface densities to receive sufficient signal intensity. The situation is partly improved by the fact that multiple binding sites at the protein complexes lead to higher stochiometric binding ratios. Different chip surfaces were tested to achieve a high immobilization density and low

nonspecific ligand adsorption. The surfaces tested included carboxymethylated dextran surface CM5, carboxymethyl dextran hydrogel surface CMD200M, linear polycarboxylate hydrogel surface HC30M and HC1500M, linear polycarboxylate hydrogel (reduced charge) surface HLC30M, and zwitterionic hydrogel surface ZC150D (**Table 2, Figs. 1-3**).

Measurements were further complicated by the concentration of analyte solutions that usually range between approximately 1/10 of K_D and 10× K_D. In the case of low-affinity binders, high nM or µM ligand concentrations often lead to strong adsorption of positively charged and hydrophobic compounds to the negatively charged chip surface, which compromises measurements. Unspecific adsorption can amount to several hundred response units (RU), thus masking binding events or making reliable quantitation impossible. As a rule of thumb, the unspecific contribution to the signal should not exceed approximately 10% of the overall signal. This can in some cases be achieved by working at very low ligand concentrations (below K_D), which results in a decrease in unspecific adsorption, and the use of a surface at which adsorption is low. For this reason, in a first test, ligands were injected for 30-60 s at a concentration of approx. 1 µM to the blank chip surface to determine the adsorption behaviour.

3.3 Multiple binding sites of small molecule ligands to Aβ42, K18 tau, full-length tau and αSyn fibrils

The measured sensorgrams reveal complex kinetics that cannot be described by a simple 1+1 kinetic model for small molecule ligands binding to Aβ, K18 tau, full-length tau and αSyn fibrils (**Figs. 1-3**). Models of higher order, including a sum of 2 and sum of 3 exponential models, were better suited, leading in most cases to good fits. Rate constants for association and dissociation, equilibrium dissociation constants, and R_{max} values are summarized in

Table 2. For αSyn fibrils, two binding sites (one high-affinity and one low-affinity) were observed for HS-169, HS-84, h-FTAA, q-FTAA, and methylene blue, of which HS-84 and HS-169 showed the most promising binding profiles (0.48 nM, 54 nM and 8.8 nM, 289 nM, respectively). For $A\beta_{42}$ fibrils, two binding sites were observed for HS-169 (139 nM, 18.2 μM) and lansoprazole (172 nM, 10.9 μM) using the Sum2Exp 2 sites fitting. Although using Sum3Exp 3 sites fitting, HS-169 showed 4.1 nM, 912 nM and 9.13 μM binding site (**STable 3**). For K18 tau fibrils, two binding sites were observed for HS-84 (452 nM, 1760 nM), q-FTAA (6.41 μM, 20.9 μM) and h-FTAA (2.81 μM, 112 μM). For full-length tau fibrils, two binding sites were observed for HS-169 (241 nM, 723 nM) and lansoprazole (1.51 μM, 8.47 μM). We observed different association and/or dissociation constants and affinities of small molecules towards immobilized $A\beta_{42}$, K18, full-length tau and αSyn fibrils by SPR. The k_{on} and k_{off} values fit with the observation of slow wash-out features of HS-169 and HS-84 reported *in vivo* (Calvo-Rodriguez et al., 2019b; Ni et al., 2022; Ni et al., 2020).

3.4 In silico modelling demonstrated multiple binding sites of LCOs on αSyn fibrils

Here, we used the 6H6B structure from the recombinant αSyn fibril, which is assembled in paired helical fibril (PHF) form. From the molecular docking studies of HS-169, HS-84, p-FTAA, and q-FTAA, we identified four binding sites on the αSyn fibril (6H6B, **Figs. 4a, b**), denoted as, sites 1-4. The salt bridge between E57 and H50 and the van der Waals interaction between the shallow hydrophobic residues (G51, A53, and V55) is found to stabilize the paired fibril in 6H6B. Site 3 is a core site inside the fibril and can be easily accessed when a limited number of molecules are used in the modelling, which might not be easily accessible in real situations. We carried out a 100-ns MD simulation for the binding of each ligand on each site, resulting in 20 trajectories with a total length of 2 μs. The ligands HS-169, HS-84, p-FTAA and q-FTAA are negatively charged; therefore, the binding affinities at site 4, which

is a positively charged site, are more favourable than those at site 3 (**Fig. 4c**). In line with the docking studies, the ranking of binding free energies indicates that HS-169 and HS-84 show very strong binding at site 4, followed by p-FTAA, q-FTAA and h-FTAA. These compounds are rich in hydrogen acceptors/donors and form stable hydrogen bonds with a cluster of positively charged residues K43, K45, H50, and K58 (**Fig. 4c**). The ligand RMSD to the initial conformation, usually used to estimate the stability of the binding, shows a deviation of larger than 8Å, which indicates that the ligand has moved away from the original binding site (**Figs. 4d-g**). From this point of view, the stability of the binding sites can be ranked as S4 > S3 > S2 > S1, for the binding the five investigated ligands. Additional in silico modelling was performed using the 2N0A αSyn structure. Four binding sites for DCVJ have been demonstrated on the 2N0A αSyn structure (Kuang et al., 2019). Here, we found a preference of these ligands for the core site 3 using the 2N0A αSyn structure (**SFigs. 3**).

3.5 Validation using immunofluorescence staining of postmortem human brain tissue and mouse models

We investigated the ligand detection of αSyn inclusions using the phospho-αSyn antibody pS129. We showed that ligands (h-FTAA, q-FTAA, and HS-169) were bound to positive pS129 αSyn inclusions in medulla oblongata and locus coeruleus tissue slices from three patients with PD (**Figs. 5a-e**). No positive signal in the non-demented control was observed (**Fig. 5f**). Colocalization of different ligands to both the Lewy neurites and Lewy bodies were observed. Next we evaluated the detection of HS-169 and HS-84 in αSyn-PFF-injected mice at 12 weeks after injection into the pedunculopontine nucleus (PPN). Positive pS129 signal was detected in the ChAT-positive cholinergic PPN neurons of αSyn-PFF-injected mice (**Fig. 5g**). Colocalization of the ligands (HS-169 and HS-84) with the pS129 signal was observed in the periaqueductal gray, nucleus accumbens, and central amygdala of αSyn-PFF-injected

mice (**Figs. 5g-j**). The somatic pS129-positive αSyn aggregates appear to be better stained by ligands compared to the neuritic pS129-positive αSyn pathology (**Fig. 5i**).

To validate the detection of Aβ or tau pathology, we studied the binding of the aforementioned ligands to transgenic mouse brains with Aβ or tau pathology. We chose transgenic mouse models to study Aβ or tau pathology since the brain tissue from AD patients commonly shows coexistence of these two pathologies. Tau mainly accumulates in the cortex and hippocampus of pR5 mice. Immunofluorescence staining performed on coronal brain tissue sections from pR5 and nontransgenic mice co-stained with anti-phospho-tau AT-8 antibody in the cortex and hippocampus confirmed the detection of PBB5 to tau inclusions (**Figs. 6a-c**). AT-100 antibody (mature phospho-tau) staining with PBB5 was performed in brain tissue slices from pR5 mice and further validated the detection (**Figs. 6a, b**).

We assessed ligand detection of Aβ deposits in brain tissue slices from arcAβ mice using 6E10. arcAβ mice develop Aβ pathology affecting both the brain parenchyma and vasculature from 6 months of age (Kecheliev et al., 2022; Knobloch et al., 2007). Immunofluorescence staining performed on coronal brain tissue sections from arcAβ and nontransgenic mice with ligands (h-FTAA, q-FTAA, and HS-169) co-stained with 6E10 (anti-$A\beta_{1-16}$) antibody further confirmed the detection of parenchymal Aβ deposits in the cortical regions (**Figs. 6d-g**).

4 Discussion

In the present work, we optimized the SPR approach to characterize the multiple binding sites of imaging ligands, and small molecule to $A\beta_{42}$, K18 tau, full-length tau and αSyn fibrils.

SPR measurements indicate that, for all fibrils, the binding kinetics of the imaging ligands and small molecules are complex since the sensorgrams recorded cannot be evaluated by fitting a simple 1+1 kinetic model. Kinetic models of higher order were better suited to fit the data, including a sum of 2 and sum of 3 exponential models. On the assumption that ligand binding to one of the 4 sites calculated for αSyn (**Fig. 4**) takes place independently, each interaction is characterized by a specific association and dissociation rate constant, resp., and relative weight. In this case, the order of the fit model should correspond to the number of binding sites. Indeed, models of higher order, in particular the sum of 3 exponentials model, considerably improved fit results as judged by chi^2 and the distribution of residuals (**Table 2**).

The fit results confirm the existence of multiple binding sites in agreement with modelling calculations. However, it needs to be noted that fitting data with models of higher order introduces considerable uncertainty due to the large number of initial parameters (k_a, k_d, R_{max} for each additional interaction: A sum of 2 (3) exponential models has at least 6 (9) free fit parameters plus (optional) a parameter for bulk response (RI) and correction (t_c). This can cause the fit routine to become stuck in local minima. This possibility can be shown by repeating a fit with a single parameter being changed by a larger value (two orders of magnitude), a procedure that often does not reproduce the initial fit. Extensive tests with the sum of 3 exponentials model revealed that fit data show low resistance to changes in the initial parameters, and the results should be interpreted with caution. The number of exponentials needed to fit a sensorgram does not necessarily correlate with the number of binding sites identified in modelling calculations. It represents its lower limit since some interactions may not be resolved due to the similarity of rate constants and a general limit of data quality of SPR measurements. For this reason, we limited the evaluation of sensorgrams to the sum2exp model, although for the sum3exp model, chi2 was often found to be much

lower, and residuals showed a more random distribution without a recognizable pattern. In the case of sensorgrams of multiple and complex interactions, calculated rate constants should be interpreted with caution.

The binding of different ligands on the various sites of these fibrils with abnormal ligand binding cavities has also been evaluated by free energy calculations to rank the affinities. In silico modelling suggested 4 binding sites on αSyn with a preference for certain binding pockets of different molecules (**Fig. 4**). The stabilities of the binding sites identified by docking were further evaluated by MD simulations and binding free energy calculations. These studies provide atomic details as well as identify key amino residues for the interaction between ligands and fibrils. One here often witnesses an induced-fit mechanism of ligand binding, e.g., enlargement of a narrow cleft in the protofibril when a large and planar ligand binds. Planarity of the ligand tends to increase its van der Waals or π-π interactions with the β-sheets of the protein and, due to a loss of molecular flexibility, an increase in fluorescence quantum yield (LIT). The core site, which is buried inside the protofibril, can often exhibit high affinities to small molecules due to enhanced van der Waals interactions. However, here we observed a surface site with strong binding affinities to the negative charged ligands due to the ionic interactions, indicating that the way the fibril twists is crucial for the existence of a site (S4) surrounded by several base residues (K43, K45, H50, and K58). In addition to the binding free energies, the residence time of the ligands at the binding sites of fibrils is also relevant to consider to rank the potency of the ligands, which can be estimated by the dissociation rate constant, k_d, measured with SPR. If a ligand can preferentially bind to the core site(s) inside the protein fibrils, as in the presently studied case, there is usually stronger binding affinity and longer wash-out time. Several recent studies have suggested 6 binding sites on Aβ fibrils (Arul Murugan et al., 2018; Balamurugan et al., 2017; Kawai et al., 2018;

Kuang et al., 2015; Murugan et al., 2016; Murugan et al., 2014) and at least 4 binding sites on tau fibrils (Kuang et al., 2020; Murugan et al., 2019; Murugan et al., 2018; Murugan et al., 2021). Kuang et al showed several surface and 3 core binding sites of PI-2620 (Kuang et al., 2020) on tau fibrils and one core and 3 surface sites on αSyn fibrils (Kuang et al., 2019).

Our affinity data of LCOs were in line with available binding data towards $A\beta_{42}$ from previous studies. Johansson et al. immobilized azide-functionalized p-FTAA and showed a K_d of ~10 nM towards $A\beta_{42}$ using SPR as well as ratiometric comparison of the excitation spectra for free vs. bound dye (Johansson et al., 2015). Using competition studies with [^{3}H]X-34, Bäck et al. showed that h-FTAA and q-FTAA bound to recombinant $A\beta_{42}$ fibrils with EC50 ~250 nM and 330–630 nM (Bäck et al., 2016). In addition, Herrmann et al. showed ratiometric comparison of the excitation spectra for free versus bound dye to determine K_d values for some LCOs bound to recombinant PrP fibrils, and the K_d values were in the low nM range (Herrmann Uli et al., 2015).

Autoradiography and in situ binding assays on brain tissues have also been used for evaluating the binding affinity, but in general, only one binding site can be obtained (Han et al., 2011). For fluorescent probes, radiometric analysis has been used to estimate the binding sites with less accuracy. Using radioligand binding assays, multiple ligand binding sites on Aβ fibrils (LeVine, 2005; Ni et al., 2017; Ni et al., 2013a; Ni et al., 2021a) and tau fibrils (Malarte et al., 2020; Ni et al., 2018; Yap et al., 2021), e.g., using THK-5351 (Lemoine et al., 2017; Lemoine et al., 2020; Stepanov et al., 2017), MK-6240 (Lemoine et al., 2021; Malarte et al., 2022; Malarte et al., 2020), and PBB3 (Ono et al., 2017), have been reported. Different tau ligands show distinct binding towards tau in AD and different primary tauopathy (Shi et

al., 2021a; Yap et al., 2021). A recent study observed a drug candidate binding to the core site of αSyn from a cryo-EM density map (Antonschmidt et al., 2022).

In addition to the affinity information, rate constants for different compounds vary by orders of magnitude for the association from ($10E^{1}$-$10E^{9}$ M^{-1} s^{-1}) and 0.1 s^{-1} to $1E^{-8}$ s^{-1} for the dissociation step (kinetic data in **Table 2**). The calculated equilibrium constants K_D are mainly in the nM to µM range, in agreement with the fact that these dyes have been successfully used in fluorescence imaging applications (Calvo-Rodriguez et al., 2019a; Ni et al., 2022; Ni et al., 2020). Some targets have components in the pM range when dissociation is very slow, including αSyn, K18 tau fibrils with h-FTAA and $A\beta_{42}$ fibril with lansoprazol. For the αSyn fibril, it is obvious to assign the components found in the analysis of sensorgrams to the binding sites calculated with molecular mechanics. In such a case, fast binding is expected to take place at sites that are easily accessible, e.g., site 1 and site 4 in **Fig 4**. In contrast, slow association and dissociation components are attributed to core site 3, which is more difficult to access. For K18 tau and $A\beta_{42}$ fibrils, no MM calculations are available. The similarity of sensorgrams between αSyn suggests that multiple binding sites should also exist in these fibrils. In light of the difficulty in comparing rate constants calculated with higher-order kinetic models, a classification of targets based on binding properties of the main component may be useful. Basically, there are two types of sensorgrams depending on whether the interaction is governed by a fast (Type 1) or slow (Type 2) association and dissociation (**Table 2**). In the case of slow dissociation and assuming that the interaction *in vivo* follows the same kinetics, the dye is most likely suitable for imaging applications. As a consequence, screening by SPR can be useful to assess whether a target is suitable for imaging applications.

We further demonstrated the colocalization of different fluorescence-emitting probes on brain tissue slices from PD patients, αSyn PFF-injected mice, and transgenic mice with Aβ plaques or tau inclusions, in line with previous observations (Ni et al., 2020; Ni et al., 2021b; Ren et al., 2022). The LCOs tested here appear to detect the αSyn inclusions in the αSyn PFF-injected mouse brain and can be useful in the *in vivo* imaging studies.

There are several limitations of our study. First, we did not use brain tissue-derived fibrils from patients with AD, primary tauopathy, PD, and MSA to investigate the ligand binding profiles. The binding sites on recombinant fibrils might differ from those on fibrils derived from patients (Lövestam et al., 2021). Further studies using fibril pulldown from human brain tissue for potential strain-dependent affinity will provide important insight because LCOs have been shown to discriminate αSyn strains in PD and MSA (Klingstedt et al., 2019; Shahnawaz et al., 2020). Second, we did not measure the binding to oligomeric forms of Aβ, tau, and αSyn by SPR due to the uncertainty of oligomer status on chips as the fibril forms rapidly. Regarding fitting of SPR data, a sum of 2 exponential models to adjust the model to the number of binding sites found in calculations resulted in data of little confidence, which is caused by the large number of free fitting parameters. Therefore, it was reasonable to expect that fitting with a sum of 4 exponential kinetic models would not lead to useful fit data.

5. Conclusion

In this work, we developed a binding property characterization platform for small molecule binding to $A\beta_{42}$, 4R tau, full-length tau and αSyn fibrils. Such a system will greatly improve the efficiency of imaging ligands and drugs targeting these protein fibrils, which are critical for the diagnosis and treatment of neurodegenerative diseases such as AD, PD, and

tauopathies. In addition, such a platform will also be potentially useful for studying competition of binding sties and off-target binding by displacement assays.

6 Declaration

Funding

RN received funding from Olga Mayenfisch Stiftung, Novartis Foundation for Medical-Biological Research, SERI (RPG_072021_02), and Swiss Center for Advanced Human Toxicity (SCAHT-AP_22_01). The in-silico modelling was enabled by resources provided the Swedish National Infrastructure for Computing (SNIC 2022-3-34) at the National Supercomputer Centre of Linköping University (Sweden) partially funded by the Swedish Research Council through grant agreement no. 2018-05973.

Competing interests

The authors declare no conflicts of interest.

Authors' contributions

The study was designed by RN. JS conducted SPR measurements and kinetic analysis. JL and HA performed and analysed the in silico modelling. JG performed the fibril production and fluorescence binding studies. BC performed staining and confocal microscopy. MH and FG provided the αSyn PFF-injected mouse brains. KPN provided the LCOs. JS, JL, and RN wrote the first draft. All authors contributed to the revision of the manuscript. All authors read and approved the final manuscript.

Acknowledgements

The authors acknowledge the Center for Microscopy and Image Analysis (ZMB), University of Zurich; Dr. Saroj Kumar Rout, Mr Patrick Vagenknecht, ETH Zurich, Prof. Jan Klohs, Institute for Biomedical Engineering, ETH Zurich/University of Zurich, and Dr. Uwe Roder at Cytiva Europe GmbH.

References

Antonschmidt, L., Matthes, D., Dervişoğlu, R., Frieg, B., Dienemann, C., Leonov, A., Nimerovsky, E., Sant, V., Ryazanov, S., Giese, A., Schröder, G.F., Becker, S., de Groot, B.L., Griesinger, C., Andreas, L.B., 2022. The clinical drug candidate anle138b binds in a cavity of lipidic α-synuclein fibrils. Nature Communications 13, 5385.

Arul Murugan, N., Zaleśny, R., Ågren, H., 2018. Unusual binding-site-specific photophysical properties of a benzothiazole-based optical probe in amyloid beta fibrils. Phys Chem Chem Phys 20, 20334-20339.

Balamurugan, K., Murugan, N.A., Långström, B., Nordberg, A., Ågren, H., 2017. Effect of Alzheimer Familial Chromosomal Mutations on the Amyloid Fibril Interaction with Different PET Tracers: Insight from Molecular Modeling Studies. ACS Chem Neurosci 8, 2655-2666.

Bankhead, P., Loughrey, M.B., Fernández, J.A., Dombrowski, Y., McArt, D.G., Dunne, P.D., McQuaid, S., Gray, R.T., Murray, L.J., Coleman, H.G., James, J.A., Salto-Tellez, M., Hamilton, P.W., 2017. QuPath: Open source software for digital pathology image analysis. Sci Rep 7, 16878.

Bian, J., Liu, Y.Q., He, J., Lin, X., Qiu, C.Y., Yu, W.B., Shen, Y., Zhu, Z.Y., Ye, D.Y., Wang, J., Chu, Y., 2021. Discovery of styrylaniline derivatives as novel alpha-synuclein aggregates ligands. Eur J Med Chem 226, 113887.

Burmann, B.M., Gerez, J.A., Matecko-Burmann, I., Campioni, S., Kumari, P., Ghosh, D., Mazur, A., Aspholm, E.E., Sulskis, D., Wawrzyniuk, M., Bock, T., Schmidt, A., Rudiger, S.G.D., Riek, R., Hiller, S., 2019. Regulation of alpha-synuclein by chaperones in mammalian cells. Nature.

Bäck, M., Appelqvist, H., LeVine, H., 3rd, Nilsson, K.P., 2016. Anionic Oligothiophenes Compete for Binding of X-34 but not PIB to Recombinant Aβ Amyloid Fibrils and Alzheimer's Disease Brain-Derived Aβ. Chemistry 22, 18335-18338.

Calvo-Rodriguez, M., Hou, S.S., Snyder, A.C., Dujardin, S., Shirani, H., Nilsson, K.P.R., Bacskai, B.J., 2019a. In vivo detection of tau fibrils and amyloid beta aggregates with luminescent conjugated oligothiophenes and multiphoton microscopy. Acta Neuropathol Commun 7, 171.

Calvo-Rodriguez, M., Hou, S.S., Snyder, A.C., Dujardin, S., Shirani, H., Nilsson, K.P.R., Bacskai, B.J., 2019b. In vivo detection of tau fibrils and amyloid β aggregates with luminescent conjugated oligothiophenes and multiphoton microscopy. Acta Neuropathologica Communications 7, 171.

De Simone, A., Mancini, F., Real Fernàndez, F., Rovero, P., Bertucci, C., Andrisano, V., 2013. Surface plasmon resonance, fluorescence, and circular dichroism studies for the characterization of the binding of BACE-1 inhibitors. Anal Bioanal Chem 405, 827-835.

Dehghani, M., Jalal, R., Rashidi, M.R., 2021. Kinetic and thermodynamic insights into the interaction of Aβ1-42 with astaxanthin and aggregation behavior of Aβ1-42: Surface plasmon resonance, microscopic, and molecular docking studies. Biophys Chem 275, 106612.

Dubois, B., Villain, N., Frisoni, G.B., Rabinovici, G.D., Sabbagh, M., Cappa, S., Bejanin, A., Bombois, S., Epelbaum, S., Teichmann, M., Habert, M.-O., Nordberg, A., Blennow, K.,

Galasko, D., Stern, Y., Rowe, C.C., Salloway, S., Schneider, L.S., Cummings, J.L., Feldman, H.H., 2021. Clinical diagnosis of Alzheimer's disease: recommendations of the International Working Group. The Lancet Neurology 20, 484-496.

Erbaş, A., Inci, F., 2022. The Role of Ligand Rebinding and Facilitated Dissociation on the Characterization of Dissociation Rates by Surface Plasmon Resonance (SPR) and Benchmarking Performance Metrics. Methods Mol Biol 2385, 237-253.

Ferrie, J.J., Lengyel-Zhand, Z., Janssen, B., Lougee, M.G., Giannakoulias, S., Hsieh, C.-J., Pagar, V.V., Weng, C.-C., Xu, H., Graham, T.J.A., Lee, V.M.Y., Mach, R.H., Petersson, E.J., 2020. Identification of a nanomolar affinity α-synuclein fibril imaging probe by ultra-high throughput in silico screening. Chemical science 11, 12746-12754.

Frenzel, D., Glück, J.M., Brener, O., Oesterhelt, F., Nagel-Steger, L., Willbold, D., 2014. Immobilization of homogeneous monomeric, oligomeric and fibrillar Aβ species for reliable SPR measurements. PLoS One 9, e89490.

Friesner, R.A., Banks, J.L., Murphy, R.B., Halgren, T.A., Klicic, J.J., Mainz, D.T., Repasky, M.P., Knoll, E.H., Shelley, M., Perry, J.K., Shaw, D.E., Francis, P., Shenkin, P.S., 2004. Glide: A New Approach for Rapid, Accurate Docking and Scoring. 1. Method and Assessment of Docking Accuracy. Journal of Medicinal Chemistry 47, 1739-1749.

Gerez, J.A., Prymaczok, N.C., Riek, R., 2020. In-Cell NMR of Intrinsically Disordered Proteins in Mammalian Cells. Methods Mol Biol 2141, 873-893.

Gerez, J.A., Prymaczok, N.C., Rockenstein, E., Herrmann, U.S., Schwarz, P., Adame, A., Enchev, R.I., Courtheoux, T., Boersema, P.J., Riek, R., Peter, M., Aguzzi, A., Masliah, E., Picotti, P., 2019. A cullin-RING ubiquitin ligase targets exogenous alpha-synuclein and inhibits Lewy body-like pathology. Sci Transl Med 11.

Gotz, J., Chen, F., van Dorpe, J., Nitsch, R.M., 2001. Formation of neurofibrillary tangles in P301l tau transgenic mice induced by Abeta 42 fibrils. Science 293, 1491-1495.

Guerrero-Ferreira, R., Taylor, N.M.I., Mona, D., Ringler, P., Lauer, M.E., Riek, R., Britschgi, M., Stahlberg, H., 2018. Cryo-EM structure of alpha-synuclein fibrils. eLife 7, e36402.

Haghaei, H., Aref Hosseini, S.R., Soltani, S., Fathi, F., Mokhtari, F., Karima, S., Rashidi, M.R., 2020. Kinetic and thermodynamic study of beta-Boswellic acid interaction with Tau protein investigated by surface plasmon resonance and molecular modeling methods. Bioimpacts 10, 17-25.

Halgren, T.A., Murphy, R.B., Friesner, R.A., Beard, H.S., Frye, L.L., Pollard, W.T., Banks, J.L., 2004. Glide: A New Approach for Rapid, Accurate Docking and Scoring. 2. Enrichment Factors in Database Screening. Journal of Medicinal Chemistry 47, 1750-1759.

Han, B.H., Zhou, M.-l., Vellimana, A.K., Milner, E., Kim, D.H., Greenberg, J.K., Chu, W., Mach, R.H., Zipfel, G.J., 2011. Resorufin analogs preferentially bind cerebrovascular amyloid: potential use as imaging ligands for cerebral amyloid angiopathy. Molecular Neurodegeneration 6, 86.

Henrich, M.T., Geibl, F.F., Lakshminarasimhan, H., Stegmann, A., Giasson, B.I., Mao, X., Dawson, V.L., Dawson, T.M., Oertel, W.H., Surmeier, D.J., 2020. Determinants of seeding and spreading of α-synuclein pathology in the brain. Sci Adv 6.

Henrich, M.T., Geibl, F.F., Lee, B., Chiu, W.H., Koprich, J.B., Brotchie, J.M., Timmermann, L., Decher, N., Matschke, L.A., Oertel, W.H., 2018. A53T-α-synuclein overexpression in murine locus coeruleus induces Parkinson's disease-like pathology in neurons and glia. Acta Neuropathol Commun 6, 39.

Herrmann Uli, S., Schütz Anne, K., Shirani, H., Huang, D., Saban, D., Nuvolone, M., Li, B., Ballmer, B., Åslund Andreas, K.O., Mason Jeffrey, J., Rushing, E., Budka, H., Nyström, S., Hammarström, P., Böckmann, A., Caflisch, A., Meier Beat, H., Nilsson, K.P.R., Hornemann, S., Aguzzi, A., 2015. Structure-based drug design identifies polythiophenes as antiprion compounds. Science Translational Medicine 7, 299ra123-299ra123.

Honarmand, S., Dabirmanesh, B., Amanlou, M., Khajeh, K., 2019. The interaction of several herbal extracts with α-synuclein: Fibril formation and surface plasmon resonance analysis. PLoS One 14, e0217801.

Hou, S.S., Yang, J., Lee, J.H., Kwon, Y., Calvo-Rodriguez, M., Bao, K., Ahn, S., Kashiwagi, S., Kumar, A.T.N., Bacskai, B.J., Choi, H.S., 2023. Near-infrared fluorescence lifetime imaging of amyloid-β aggregates and tau fibrils through the intact skull of mice. Nat Biomed Eng.

Jha, N.N., Kumar, R., Panigrahi, R., Navalkar, A., Ghosh, D., Sahay, S., Mondal, M., Kumar, A., Maji, S.K., 2017. Comparison of α-Synuclein Fibril Inhibition by Four Different Amyloid Inhibitors. ACS Chem Neurosci 8, 2722-2733.

Johansson, L.B.G., Simon, R., Bergström, G., Eriksson, M., Prokop, S., Mandenius, C.F., Heppner, F.L., Åslund, A.K.O., Nilsson, K.P.R., 2015. An azide functionalized oligothiophene ligand--a versatile tool for multimodal detection of disease associated protein aggregates. Biosens Bioelectron 63, 204-211.

Jorgensen, W.L., Chandrasekhar, J., Madura, J.D., Impey, R.W., Klein, M.L., 1983. Comparison of simple potential functions for simulating liquid water. The Journal of Chemical Physics 79, 926-935.

Jucker, M., Walker, L.C., 2018. Propagation and spread of pathogenic protein assemblies in neurodegenerative diseases. Nature Neuroscience 21, 1341-1349.

Karlsson, R., 2004. SPR for molecular interaction analysis: a review of emerging application areas. J Mol Recognit 17, 151-161.

Karlsson, R., Katsamba, P.S., Nordin, H., Pol, E., Myszka, D.G., 2006. Analyzing a kinetic titration series using affinity biosensors. Analytical Biochemistry 349, 136-147.

Kawai, R., Araki, M., Yoshimura, M., Kamiya, N., Ono, M., Saji, H., Okuno, Y., 2018. Core Binding Site of a Thioflavin-T-Derived Imaging Probe on Amyloid β Fibrils Predicted by Computational Methods. ACS Chem Neurosci 9, 957-966.

Kecheliev, V., Spinelli, F., Herde, A., Haider, A., Mu, L., Klohs, J., Ametamey, S.M., Ni, R., 2022. Evaluation of cannabinoid type 2 receptor expression and pyridine-based radiotracers in brains from a mouse model of Alzheimer's disease. Frontiers in Aging Neuroscience 14.

Kim, S., Wark, A.W., Lee, H.J., 2016. Femtomolar Detection of Tau Proteins in Undiluted Plasma Using Surface Plasmon Resonance. Anal Chem 88, 7793-7799.

Klingstedt, T., Aslund, A., Simon, R.A., Johansson, L.B., Mason, J.J., Nystrom, S., Hammarstrom, P., Nilsson, K.P., 2011. Synthesis of a library of oligothiophenes and their utilization as fluorescent ligands for spectral assignment of protein aggregates. Organic & biomolecular chemistry 9, 8356-8370.

Klingstedt, T., Ghetti, B., Holton, J.L., Ling, H., Nilsson, K.P.R., Goedert, M., 2019. Luminescent conjugated oligothiophenes distinguish between α-synuclein assemblies of Parkinson's disease and multiple system atrophy. Acta Neuropathologica Communications 7, 193.

Knobloch, M., Konietzko, U., Krebs, D.C., Nitsch, R.M., 2007. Intracellular Aβ and cognitive deficits precede β-amyloid deposition in transgenic arcAβ mice. Neurobiology of Aging 28, 1297-1306.

Kollman, P.A., Massova, I., Reyes, C., Kuhn, B., Huo, S., Chong, L., Lee, M., Lee, T., Duan, Y., Wang, W., Donini, O., Cieplak, P., Srinivasan, J., Case, D.A., Cheatham, T.E., 2000. Calculating Structures and Free Energies of Complex Molecules: Combining Molecular Mechanics and Continuum Models. Accounts of Chemical Research 33, 889-897.

Krishnaswamy, S., Lin, Y., Rajamohamedsait, W.J., Rajamohamedsait, H.B., Krishnamurthy, P., Sigurdsson, E.M., 2014. Antibody-derived in vivo imaging of tau pathology. The Journal of neuroscience : the official journal of the Society for Neuroscience 34, 16835-16850.

Kuang, G., Murugan, N.A., Tu, Y., Nordberg, A., Ågren, H., 2015. Investigation of the Binding Profiles of AZD2184 and Thioflavin T with Amyloid-β(1-42) Fibril by Molecular Docking and Molecular Dynamics Methods. J Phys Chem B 119, 11560-11567.
Kuang, G., Murugan, N.A., Zhou, Y., Nordberg, A., Ågren, H., 2020. Computational Insight into the Binding Profile of the Second-Generation PET Tracer PI2620 with Tau Fibrils. ACS Chem Neurosci 11, 900-908.
Kuang, G., Murugan, N.A., Ågren, H., 2019. Mechanistic Insight into the Binding Profile of DCVJ and α-Synuclein Fibril Revealed by Multiscale Simulations. ACS Chemical Neuroscience 10, 610-617.
Kuchibhotla, K.V., Wegmann, S., Kopeikina, K.J., Hawkes, J., Rudinskiy, N., Andermann, M.L., Spires-Jones, T.L., Bacskai, B.J., Hyman, B.T., 2014. Neurofibrillary tangle-bearing neurons are functionally integrated in cortical circuits in vivo. Proceedings of the National Academy of Sciences 111, 510-514.
Kuebler, L., Buss, S., Leonov, A., Ryazanov, S., Schmidt, F., Maurer, A., Weckbecker, D., Landau, A.M., Lillethorup, T.P., Bleher, D., Saw, R.S., Pichler, B.J., Griesinger, C., Giese, A., Herfert, K., 2021. [(11)C]MODAG-001-towards a PET tracer targeting α-synuclein aggregates. Eur J Nucl Med Mol Imaging 48, 1759-1772.
Kumari, P., Ghosh, D., Vanas, A., Fleischmann, Y., Wiegand, T., Jeschke, G., Riek, R., Eichmann, C., 2021. Structural insights into α-synuclein monomer-fibril interactions. Proc Natl Acad Sci U S A 118.
Lemoine, L., Gillberg, P.G., Bogdanovic, N., Nennesmo, I., Saint-Aubert, L., Viitanen, M., Graff, C., Ingelsson, M., Nordberg, A., 2021. Amyloid, tau, and astrocyte pathology in autosomal-dominant Alzheimer's disease variants: AβPParc and PSEN1DE9. Mol Psychiatry 26, 5609-5619.
Lemoine, L., Gillberg, P.G., Svedberg, M., Stepanov, V., Jia, Z., Huang, J., Nag, S., Tian, H., Ghetti, B., Okamura, N., Higuchi, M., Halldin, C., Nordberg, A., 2017. Comparative binding properties of the tau PET tracers THK5117, THK5351, PBB3, and T807 in postmortem Alzheimer brains. Alzheimers Res Ther 9, 96.
Lemoine, L., Ledreux, A., Mufson, E.J., Perez, S.E., Simic, G., Doran, E., Lott, I., Carroll, S., Bharani, K., Thomas, S., Gilmore, A., Hamlett, E.D., Nordberg, A., Granholm, A.C., 2020. Regional binding of tau and amyloid PET tracers in Down syndrome autopsy brain tissue. Mol Neurodegener 15, 68.
LeVine, H., 3rd, 2005. Multiple ligand binding sites on A beta(1-40) fibrils. Amyloid 12, 5-14.
Li, J., Abel, R., Zhu, K., Cao, Y., Zhao, S., Friesner, R.A., 2011. The VSGB 2.0 model: A next generation energy model for high resolution protein structure modeling. Proteins: Structure, Function, and Bioinformatics 79, 2794-2812.
Lisi, S., Scarano, S., Fedeli, S., Pascale, E., Cicchi, S., Ravelet, C., Peyrin, E., Minunni, M., 2017. Toward sensitive immuno-based detection of tau protein by surface plasmon resonance coupled to carbon nanostructures as signal amplifiers. Biosens Bioelectron 93, 289-292.
Lu, C., Wu, C., Ghoreishi, D., Chen, W., Wang, L., Damm, W., Ross, G.A., Dahlgren, M.K., Russell, E., Von Bargen, C.D., Abel, R., Friesner, R.A., Harder, E.D., 2021. OPLS4: Improving Force Field Accuracy on Challenging Regimes of Chemical Space. Journal of Chemical Theory and Computation 17, 4291-4300.
Lövestam, S., Schweighauser, M., Matsubara, T., Murayama, S., Tomita, T., Ando, T., Hasegawa, K., Yoshida, M., Tarutani, A., Hasegawa, M., Goedert, M., Scheres, S.H.W., 2021. Seeded assembly in vitro does not replicate the structures of α-synuclein filaments from multiple system atrophy. FEBS open bio 11, 999-1013.

Malarte, M.L., Gillberg, P.G., Kumar, A., Bogdanovic, N., Lemoine, L., Nordberg, A., 2022. Discriminative binding of tau PET tracers PI2620, MK6240 and RO948 in Alzheimer's disease, corticobasal degeneration and progressive supranuclear palsy brains. Mol Psychiatry.
Malarte, M.L., Nordberg, A., Lemoine, L., 2020. Characterization of MK6240, a tau PET tracer, in autopsy brain tissue from Alzheimer's disease cases. Eur J Nucl Med Mol Imaging.
Marasco, D., Vicidomini, C., Krupa, P., Cioffi, F., Huy, P.D.Q., Li, M.S., Florio, D., Broersen, K., De Pandis, M.F., Roviello, G.N., 2021. Plant isoquinoline alkaloids as potential neurodrugs: A comparative study of the effects of benzo[c]phenanthridine and berberine-based compounds on β-amyloid aggregation. Chem Biol Interact 334, 109300.
Martins, A.F., Dias, D.M., Morfin, J.-F., Lacerda, S., Laurents, D.V., Tóth, É., Geraldes, C.F.G.C., 2015. Interaction of PiB-Derivative Metal Complexes with Beta-Amyloid Peptides: Selective Recognition of the Aggregated Forms. Chemistry – A European Journal 21, 5413-5422.
Martyna, G.J., Klein, M.L., Tuckerman, M., 1992. Nosé–Hoover chains: The canonical ensemble via continuous dynamics. The Journal of Chemical Physics 97, 2635-2643.
Martyna, G.J., Tobias, D.J., Klein, M.L., 1994. Constant pressure molecular dynamics algorithms. The Journal of Chemical Physics 101, 4177-4189.
Massalimova, A., Ni, R., Nitsch, R.M., Reisert, M., von Elverfeldt, D., Klohs, J., 2021. Diffusion Tensor Imaging Reveals Whole-Brain Microstructural Changes in the P301L Mouse Model of Tauopathy. Neurodegener Dis, 1-12.
Matsuoka, K., Ono, M., Takado, Y., Hirata, K., Endo, H., Ohfusa, T., Kojima, T., Yamamoto, T., Onishi, T., Orihara, A., Tagai, K., Takahata, K., Seki, C., Shinotoh, H., Kawamura, K., Shimizu, H., Shimada, H., Kakita, A., Zhang, M.R., Suhara, T., Higuchi, M., 2022. High-Contrast Imaging of α-Synuclein Pathologies in Living Patients with Multiple System Atrophy, Mov Disord, United States, pp. 2159-2161.
McMurray, L., Macdonald, J.A., Ramakrishnan, N.K., Zhao, Y., Williamson, D.W., Tietz, O., Zhou, X., Kealey, S., Fagan, S.G., Smolek, T., Cubinkova, V., Žilka, N., Spillantini, M.G., Tolkovsky, A.M., Goedert, M., Aigbirhio, F.I., 2021. Synthesis and Assessment of Novel Probes for Imaging Tau Pathology in Transgenic Mouse and Rat Models. ACS Chem Neurosci 12, 1885-1893.
Murugan, N.A., Chiotis, K., Rodriguez-Vieitez, E., Lemoine, L., Ågren, H., Nordberg, A., 2019. Cross-interaction of tau PET tracers with monoamine oxidase B: evidence from in silico modelling and in vivo imaging. Eur J Nucl Med Mol Imaging 46, 1369-1382.
Murugan, N.A., Halldin, C., Nordberg, A., Långström, B., Ågren, H., 2016. The Culprit Is in the Cave: The Core Sites Explain the Binding Profiles of Amyloid-Specific Tracers. J Phys Chem Lett 7, 3313-3321.
Murugan, N.A., Nordberg, A., Ågren, H., 2018. Different Positron Emission Tomography Tau Tracers Bind to Multiple Binding Sites on the Tau Fibril: Insight from Computational Modeling. ACS Chem Neurosci 9, 1757-1767.
Murugan, N.A., Nordberg, A., Ågren, H., 2021. Cryptic Sites in Tau Fibrils Explain the Preferential Binding of the AV-1451 PET Tracer toward Alzheimer's Tauopathy. ACS Chemical Neuroscience.
Murugan, N.A., Zaleśny, R., Kongsted, J., Nordberg, A., Ågren, H., 2014. Promising two-photon probes for in vivo detection of β amyloid deposits. Chem Commun (Camb) 50, 11694-11697.
Nangare, S., Patil, P., 2021. Nanoarchitectured Bioconjugates and Bioreceptors Mediated Surface Plasmon Resonance Biosensor for In Vitro Diagnosis of Alzheimer's Disease: Development and Future Prospects. Crit Rev Anal Chem, 1-31.
Ni, R., Chen, Z., Deán-Ben, X.L., Voigt, F.F., Kirschenbaum, D., Shi, G., Villois, A., Zhou, Q., Crimi, A., Arosio, P., Nitsch, R.M., Nilsson, K.P.R., Aguzzi, A., Helmchen, F., Klohs, J.,

Razansky, D., 2022. Multiscale optical and optoacoustic imaging of amyloid-β deposits in mice. Nature Biomedical Engineering.

Ni, R., Chen, Z., Gerez, J.A., Shi, G., Zhou, Q., Riek, R., Nilsson, K.P.R., Razansky, D., Klohs, J., 2020. Detection of cerebral tauopathy in P301L mice using high-resolution large-field multifocal illumination fluorescence microscopy. Biomed Opt Express 11, 4989-5002.

Ni, R., Gillberg, P.-G., Bogdanovic, N., Viitanen, M., Myllykangas, L., Nennesmo, I., Långström, B., Nordberg, A., 2017. Amyloid tracers binding sites in autosomal dominant and sporadic Alzheimer's disease. Alzheimer's & Dementia 13, 419-430.

Ni, R., Gillberg, P.G., Bergfors, A., Marutle, A., Nordberg, A., 2013a. Amyloid tracers detect multiple binding sites in Alzheimer's disease brain tissue. Brain 136, 2217-2227.

Ni, R., Ji, B., Ono, M., Sahara, N., Zhang, M.R., Aoki, I., Nordberg, A., Suhara, T., Higuchi, M., 2018. Comparative in-vitro and in-vivo quantifications of pathological tau deposits and their association with neurodegeneration in tauopathy mouse models. J Nucl Med 59, 960-966.

Ni, R., Marutle, A., Nordberg, A., 2013b. Modulation of α7 nicotinic acetylcholine receptor and fibrillar amyloid-β interactions in Alzheimer's disease brain. J Alzheimers Dis 33, 841-851.

Ni, R., Röjdner, J., Voytenko, L., Dyrks, T., Thiele, A., Marutle, A., Nordberg, A., 2021a. In vitro Characterization of the Regional Binding Distribution of Amyloid PET Tracer Florbetaben and the Glia Tracers Deprenyl and PK11195 in Autopsy Alzheimer's Brain Tissue. J Alzheimers Dis 80, 1723-1737.

Ni, R., Villois, A., Dean-Ben, X.L., Chen, Z., Vaas, M., Stavrakis, S., Shi, G., deMello, A., Ran, C., Razansky, D., Arosio, P., Klohs, J., 2021b. In-vitro and in-vivo characterization of CRANAD-2 for multi-spectral optoacoustic tomography and fluorescence imaging of amyloid-beta deposits in Alzheimer mice. Photoacoustics 23, 100285.

Ono, M., Sahara, N., Kumata, K., Ji, B., Ni, R., Koga, S., Dickson, D.W., Trojanowski, J.Q., Lee, V.M.Y., Yoshida, M., Hozumi, I., Yoshiyama, Y., Van Swieten, J.C., Nordberg, A., Suhara, T., Zhang, M.R., Higuchi, M., 2017. Distinct binding of PET ligands PBB3 and AV-1451 to tau fibril strains in neurodegenerative tauopathies. Brain 140, 764-780.

Ren, W., Li, L., Zhang, J., Vaas, M., Klohs, J., Ripoll, J., Wolf, M., Ni, R., Rudin, M., 2022. Non-invasive visualization of amyloid-beta deposits in Alzheimer amyloidosis mice using magnetic resonance imaging and fluorescence molecular tomography. Biomed Opt Express 13, 3809-3822.

Reyes, J.F., Ekmark-Léwen, S., Perdiki, M., Klingstedt, T., Hoffmann, A., Wiechec, E., Nilsson, P., Nilsson, K.P.R., Alafuzoff, I., Ingelsson, M., Hallbeck, M., 2021. Accumulation of alpha-synuclein within the liver, potential role in the clearance of brain pathology associated with Parkinson's disease. Acta Neuropathol Commun 9, 46.

Rezabakhsh, A., Rahbarghazi, R., Fathi, F., 2020. Surface plasmon resonance biosensors for detection of Alzheimer's biomarkers; an effective step in early and accurate diagnosis. Biosens Bioelectron 167, 112511.

Riek, R., Eisenberg, D.S., 2016. The activities of amyloids from a structural perspective. Nature 539, 227-235.

Rojo, L.E., Alzate-Morales, J., Saavedra, I.N., Davies, P., Maccioni, R.B., 2010. Selective interaction of lansoprazole and astemizole with tau polymers: potential new clinical use in diagnosis of Alzheimer's disease. Journal of Alzheimer's disease : JAD 19, 573-589.

Ryu, J., Joung, H.A., Kim, M.G., Park, C.B., 2008. Surface plasmon resonance analysis of Alzheimer's beta-amyloid aggregation on a solid surface: from monomers to fully-grown fibrils. Anal Chem 80, 2400-2407.

Sangwan, S., Sahay, S., Murray, K.A., Morgan, S., Guenther, E.L., Jiang, L., Williams, C.K., Vinters, H.V., Goedert, M., Eisenberg, D.S., 2020. Inhibition of synucleinopathic seeding by rationally designed inhibitors. Elife 9.

Sanna, E., Rodrigues, M., Fagan, S.G., Chisholm, T.S., Kulenkampff, K., Klenerman, D., Spillantini, M.G., Aigbirhio, F.I., Hunter, C.A., 2021. Mapping the binding site topology of amyloid protein aggregates using multivalent ligands. Chem Sci 12, 8892-8899.

Schütz, A.K., Hornemann, S., Wälti, M.A., Greuter, L., Tiberi, C., Cadalbert, R., Gantner, M., Riek, R., Hammarström, P., Nilsson, K.P.R., Böckmann, A., Aguzzi, A., Meier, B.H., 2018. Binding of Polythiophenes to Amyloids: Structural Mapping of the Pharmacophore. ACS Chem Neurosci 9, 475-481.

Shahnawaz, M., Mukherjee, A., Pritzkow, S., Mendez, N., Rabadia, P., Liu, X., Hu, B., Schmeichel, A., Singer, W., Wu, G., Tsai, A.-L., Shirani, H., Nilsson, K.P.R., Low, P.A., Soto, C., 2020. Discriminating α-synuclein strains in Parkinson's disease and multiple system atrophy. Nature 578, 273-277.

Shi, Y., Murzin, A., Falcon, B., Epstein, A., Machin, J., Tempest, P., Newell, K., Vidal, R., Garringer, H., Sahara, N., Higuchi, M., Ghetti, B., Jang, M.-K., Scheres, S., Goedert, M., 2021a. Cryo-EM structures of tau filaments from Alzheimer's disease with PET ligand APN-1607. Acta Neuropathol., 1-12.

Shi, Y., Zhang, W., Yang, Y., Murzin, A.G., Falcon, B., Kotecha, A., van Beers, M., Tarutani, A., Kametani, F., Garringer, H.J., Vidal, R., Hallinan, G.I., Lashley, T., Saito, Y., Murayama, S., Yoshida, M., Tanaka, H., Kakita, A., Ikeuchi, T., Robinson, A.C., Mann, D.M.A., Kovacs, G.G., Revesz, T., Ghetti, B., Hasegawa, M., Goedert, M., Scheres, S.H.W., 2021b. Structure-based classification of tauopathies. Nature.

Shimogawa, M., Petersson, E.J., 2021. New strategies for fluorescently labeling proteins in the study of amyloids. Curr Opin Chem Biol 64, 57-66.

Shirani, H., Linares, M., Sigurdson, C.J., Lindgren, M., Norman, P., Nilsson, K.P., 2015. A Palette of Fluorescent Thiophene-Based Ligands for the Identification of Protein Aggregates. Chemistry 21, 15133-15137.

Smith, R., Capotosti, F., Schain, M., Ohlsson, T., Touilloux, T., Hliva, V., Vokali, E., Luthi-Carter, R., Molette, J., Dimitrakopoulos, I.K., Jögi, J., Stomrud, E., Hall, S., Bratteby, K., Tampio, E., Pfeifer, A., Kosco-Vilbois, M., Streffer, J., Hansson, O., 2022. Initial clinical scans using [18F]ACI-12589, a novel α-synuclein PET-tracer. Alzheimer's & Dementia 18, e065394.

Spillantini, M.G., Goedert, M., 2013. Tau pathology and neurodegeneration. The Lancet. Neurology 12, 609-622.

Stepanov, V., Svedberg, M., Jia, Z., Krasikova, R., Lemoine, L., Okamura, N., Furumoto, S., Mitsios, N., Mulder, J., Långström, B., Nordberg, A., Halldin, C., 2017. Development of [(11)C]/[(3)H]THK-5351 - A potential novel carbon-11 tau imaging PET radioligand. Nucl Med Biol 46, 50-53.

Stravalaci, M., Bastone, A., Beeg, M., Cagnotto, A., Colombo, L., Di Fede, G., Tagliavini, F., Cantù, L., Del Favero, E., Mazzanti, M., Chiesa, R., Salmona, M., Diomede, L., Gobbi, M., 2012. Specific recognition of biologically active amyloid-β oligomers by a new surface plasmon resonance-based immunoassay and an in vivo assay in Caenorhabditis elegans. J Biol Chem 287, 27796-27805.

Stravalaci, M., Beeg, M., Salmona, M., Gobbi, M., 2011. Use of surface plasmon resonance to study the elongation kinetics and the binding properties of the highly amyloidogenic Aβ(1-42) peptide, synthesized by depsi-peptide technique. Biosens Bioelectron 26, 2772-2775.

Tanriöver, G., Bacioglu, M., Schweighauser, M., Mahler, J., Wegenast-Braun, B.M., Skodras, A., Obermüller, U., Barth, M., Kronenberg-Versteeg, D., Nilsson, K.P.R., Shimshek, D.R., Kahle, P.J., Eisele, Y.S., Jucker, M., 2020. Prominent microglial inclusions in transgenic

mouse models of α-synucleinopathy that are distinct from neuronal lesions. Acta Neuropathol Commun 8, 133.

Thom, T., Schmitz, M., Fischer, A.L., Correia, A., Correia, S., Llorens, F., Pique, A.V., Möbius, W., Domingues, R., Zafar, S., Stoops, E., Silva, C.J., Fischer, A., Outeiro, T.F., Zerr, I., 2021. Cellular Prion Protein Mediates α-Synuclein Uptake, Localization, and Toxicity In Vitro and In Vivo. Mov Disord.

Torre-Muruzabal, T., Van der Perren, A., Coens, A., Gelders, G., Janer, A.B., Camacho-Garcia, S., Klingstedt, T., Nilsson, P., Stefanova, N., Melki, R., Baekelandt, V., Peelaerts, W., 2023. Host oligodendrogliopathy and α-synuclein strains dictate disease severity in multiple system atrophy. Brain 146, 237-251.

Vagenknecht, P., Luzgin, A., Ono, M., Ji, B., Higuchi, M., Noain, D., Maschio, C.A., Sobek, J., Chen, Z., Konietzko, U., Gerez, J.A., Riek, R., Razansky, D., Klohs, J., Nitsch, R.M., Dean-Ben, X.L., Ni, R., 2022. Non-invasive imaging of tau-targeted probe uptake by whole brain multi-spectral optoacoustic tomography. Eur J Nucl Med Mol Imaging.

Verwilst, P., Kim, H.-R., Seo, J., Sohn, N.-W., Cha, S.-Y., Kim, Y., Maeng, S., Shin, J.-W., Kwak, J.H., Kang, C., Kim, J.S., 2017. Rational Design of in Vivo Tau Tangle-Selective Near-Infrared Fluorophores: Expanding the BODIPY Universe. Journal of the American Chemical Society 139, 13393-13403.

Wu, Q., Lin, Y., Gu, J., Sigurdsson, E., 2018. Dynamic assessment of tau immunotherapies in the brains of live animals by two-photon imaging. EBioMedicine 35.

Yang, Y., Arseni, D., Zhang, W., Huang, M., Lövestam, S., Schweighauser, M., Kotecha, A., Murzin, A.G., Peak-Chew, S.Y., Macdonald, J., Lavenir, I., Garringer, H.J., Gelpi, E., Newell, K.L., Kovacs, G.G., Vidal, R., Ghetti, B., Ryskeldi-Falcon, B., Scheres, S.H.W., Goedert, M., 2022. Cryo-EM structures of amyloid-β 42 filaments from human brains. Science 375, 167-172.

Yap, S.Y., Frias, B., Wren, M.C., Schöll, M., Fox, N.C., Årstad, E., Lashley, T., Sander, K., 2021. Discriminatory ability of next-generation tau PET tracers for Alzheimer's disease. Brain.

Yin, Z., Cheng, X., Wang, G., Chen, J., Jin, Y., Tu, Q., Xiang, J., 2020. SPR immunosensor combined with Ti(4+)@TiP nanoparticles for the evaluation of phosphorylated alpha-synuclein level. Mikrochim Acta 187, 509.

Zhou, Y., Li, J., Nordberg, A., Ågren, H., 2021. Dissecting the Binding Profile of PET Tracers to Corticobasal Degeneration Tau Fibrils. ACS Chem Neurosci 12, 3487-3496.

Figure legends

Fig. 1 Binding data on recombinant alpha-synuclein fibrils using different surface plasmon resonance and in silico modelling of multiple binding sites. (**a**) Western blot characterization of αSyn using Anti-α-Synuclein antibody, Mouse monoclonal, clone Syn211; (**b**) TEM of αSyn fibril; (**c**) thioflavin T assay on αSyn (green) and blank (dd. water, gray) using spectrofluorometric measurements. (**d-g**) Sensorgrams of αSyn fibrils covalently immobilized on sensor chips with a 3D-hydrogel chip surface. Analytes including q-FTAA (d), h-FTAA (e), HS-169 (f), HS-84 (g), PBB5 (h), and methylene blue (i) were investigated. Black line (experimental data). Red line (fitting curve). Details on chip, chip surface, K_d evaluation in Table 1.

Fig. 2 SPR binding data on recombinant K18 tau and full-length tau fibrils using surface plasmon resonance. (**a**) Western blot characterization of K18 tau and full-length tau using Anti-Tau (RD4) Antibody, clone 1E1/A6; (**b**) TEM of K18 tau and full-length tau fibrils; (**c, d**) Thioflavin T assay of K18 tau fibril (red) and full-length tau fibril (purple) and blank (dd. Water, gray) using spectrofluorometric measurements; (**e-i**) Sensorgrams of K18 tau fibrils covalently immobilized on a sensor chip with a 3D-hydrogel chip surface. Analytes including q-FTAA (e), h-FTAA (f), HS-169 (g), HS-84 (h), and methylene blue (i) were investigated. (**j-l**) Sensorgrams of full-length tau fibrils covalently immobilized on a sensor chip with a 3D-hydrogel chip surface. Analytes including HS-84 (j), HS-169 (k), and lansoprazole (l) were investigated. Black line (experimental data). Red line (fitting curve). Details on chip, chip surface, K_d evaluation in Table 1.

Fig. 3 SPR binding data on recombinant $A\beta_{42}$ fibrils using surface plasmon resonance. (**a**) Western blot characterization of $A\beta_{42}$ using monoclonal Anti-β-amyloid antibody, clone BAM-10; (**b**) TEM of $A\beta_{42}$ fibril; (**c**) Thioflavin T assay of $A\beta_{42}$ fibril (blue) and blank (dd. Water, gray) using spectrofluorometric measurements; (**d-f**) Sensorgrams of $A\beta_{42}$ fibrils covalently immobilized on a sensor chip with a 3D-hydrogel chip surface ZC150D. Analytes including HS-169, HS-84 and lansoprazole were investigated. Black line (experimental data). Red line (fitting curve). Details on chip, chip surface, K_d evaluation in Table 1.

Fig. 4. **In silico modelling of the binding sites of HS-169, HS-84, h-FTAA, p-FTAA and q-FTAA on the 6H6B alpha-synuclein structure.** (**a**) Four binding sites (S1-S4) on alpha-synuclein fibrils; the red circle indicates the location of another site 4; (**b**) Zoomed-in view of h-FTAA binding to site 4. (**c**) MM/GBSA calculation of free energy indicating that site 4 is preferred by HS-169, HS-84, h-FTAA, p-FTAA and q-FTAA. (**d-g**) RMSD analysis of the ligands binding to 4 binding sites (S1-S4).

Fig 5. Confocal imaging of alpha-synuclein inclusions in brain tissue sections from PD patients and αSyn PFF-injected mice. (**a-d**) Immunofluorescence staining in the medulla oblongata of PD patients. αSyn-positive Lewy neurites (*) and αSyn-positive Lewy body (arrowhead). Colocalization of Alexa488-anti-aSYN phosphor S129 antibody pS129 (green), with h-FTAA (yellow), HS-169 (cyan), and q-FTAA (magenta); Nuclei were counterstained using DAPI (white). (**e-h**) Immunofluorescence staining in αSyn PFF-injected mouse brain. pS129-positive inclusions in ChAT-positive neurons (yellow) in the PPN of αSyn PFF-injected mice. (**f-g**) Colocalization of pS129-positive inclusions (green) with the ligand HS-169 (cyan) in the periaqueductal gray matter (PAG, h is Zoom-in-view of g). **(h**) Colocalization of pS129-positive inclusions (green) with HS-84 (red) in the nucleus accumbens (NAc); nuclei were counterstained using DAPI (white). Scale bar = 50 μm (c, e), 10 μm (a, b, d, f, g, h).

Fig. 6 Colocalization of imaging ligands with tau and amyloid-beta. (**a-c**) Immunofluorescence staining in the hippocampus of pR5 tau mice. Alexa488-AT8 (red), Alexa488-AT100 (magenta), h-FTAA (green), PBB5 (yellow), HS-169 (cyan); nuclei were counterstained using DAPI (white). Scale bar = 10 μm. (**d-g**) Amyloid-beta deposits in the cortex of arcAβ mouse brain tissue sections. Anti-$A\beta_{1\text{-}16}$ antibody Alexa488-6E10 (green), HS-84 (red), h-FTAA (yellow), q-FTAA (magenta), HS-169 (cyan). Nuclei were counterstained using DAPI (white). Scale bar = 50 μm (d, f, g), 10 μm (a, b, c, e).

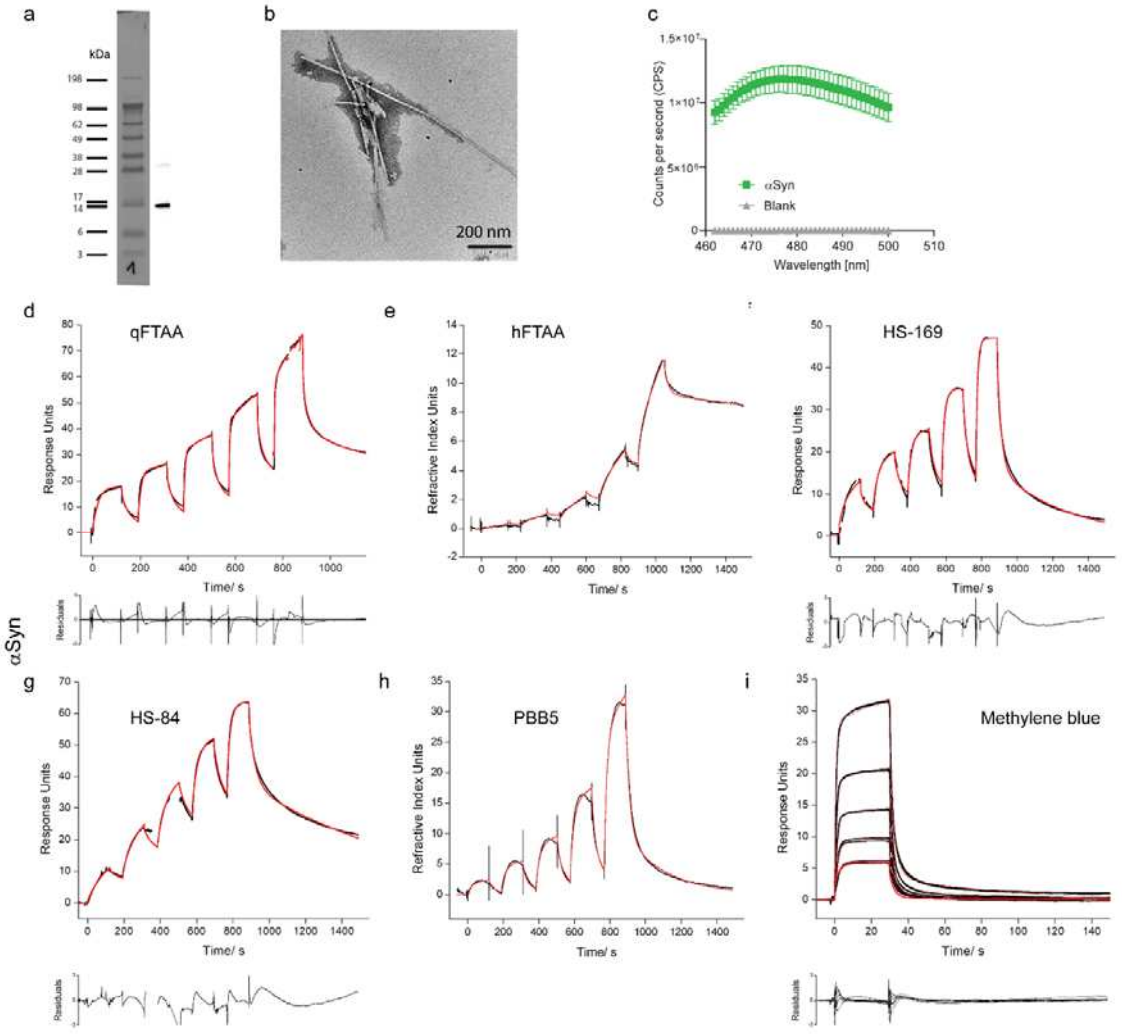

Fig. 1

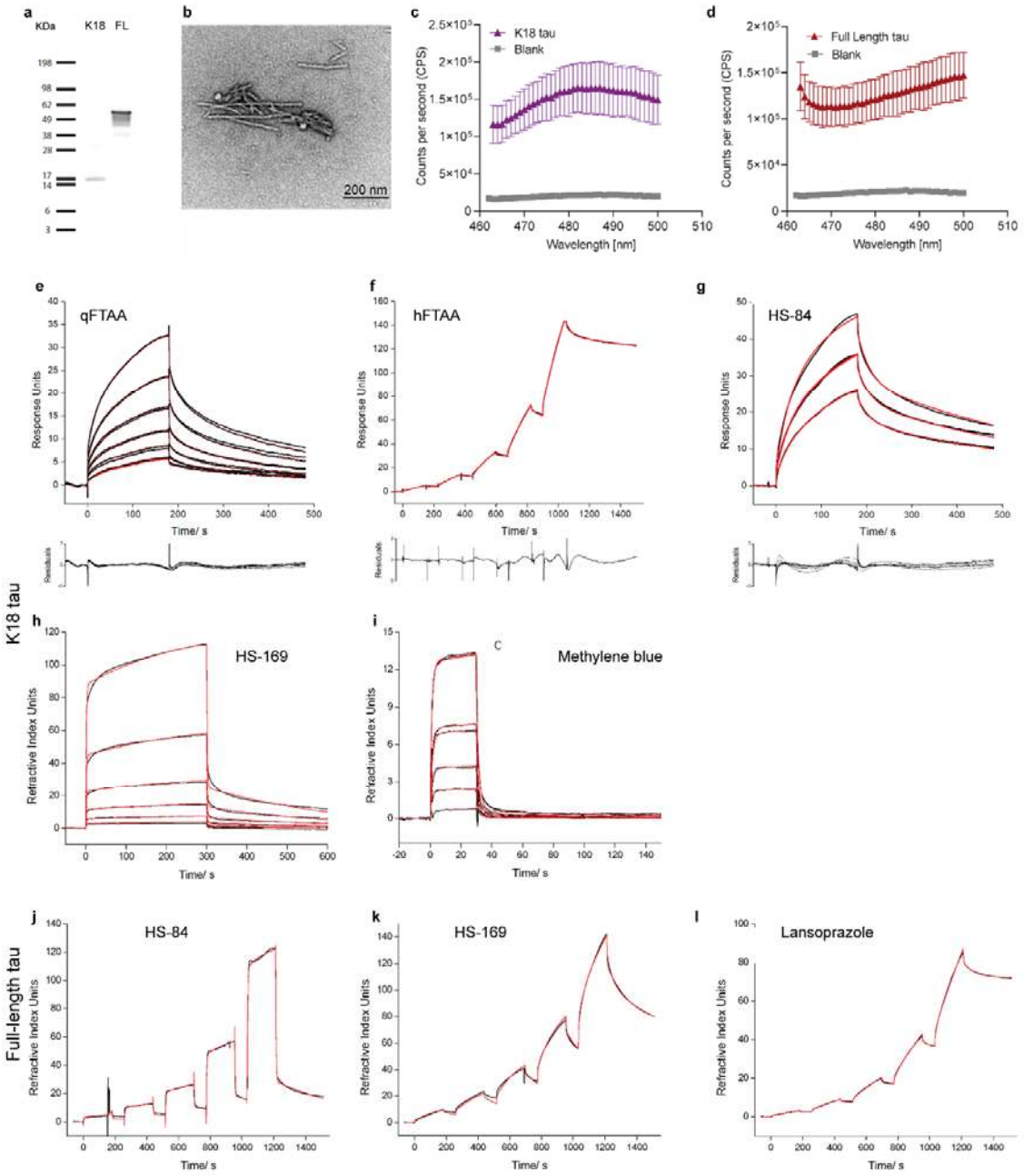

Fig. 2

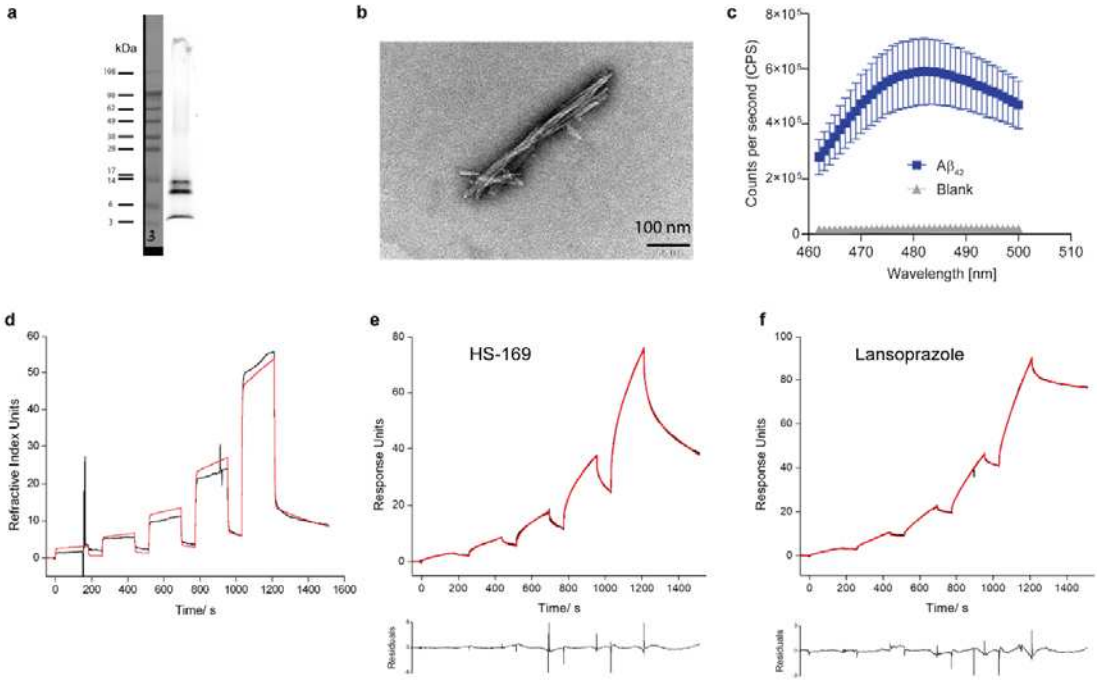

Fig. 3

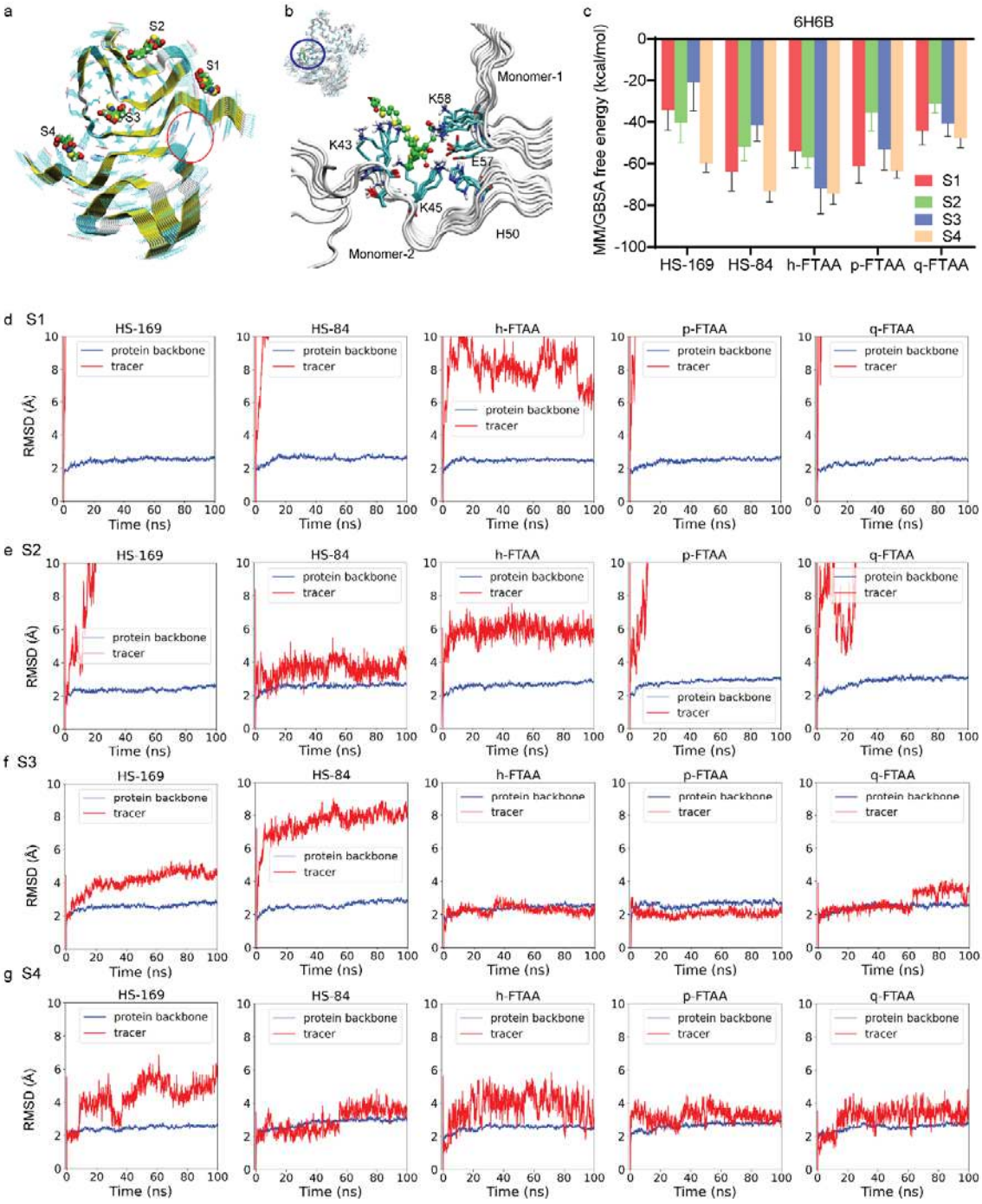

Fig. 4

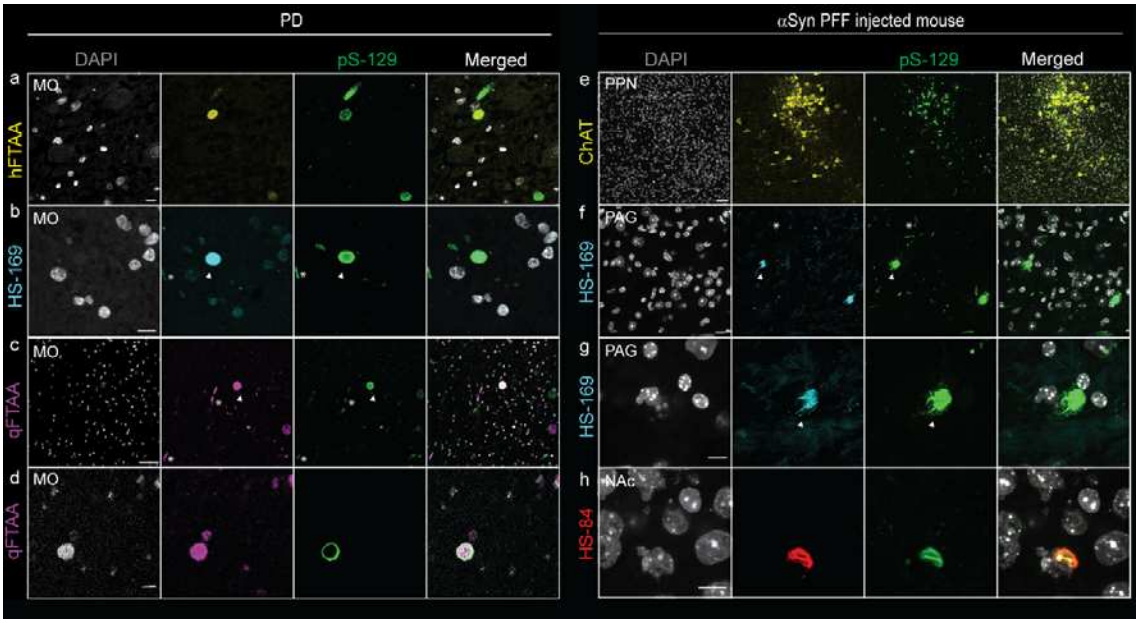

Fig. 5

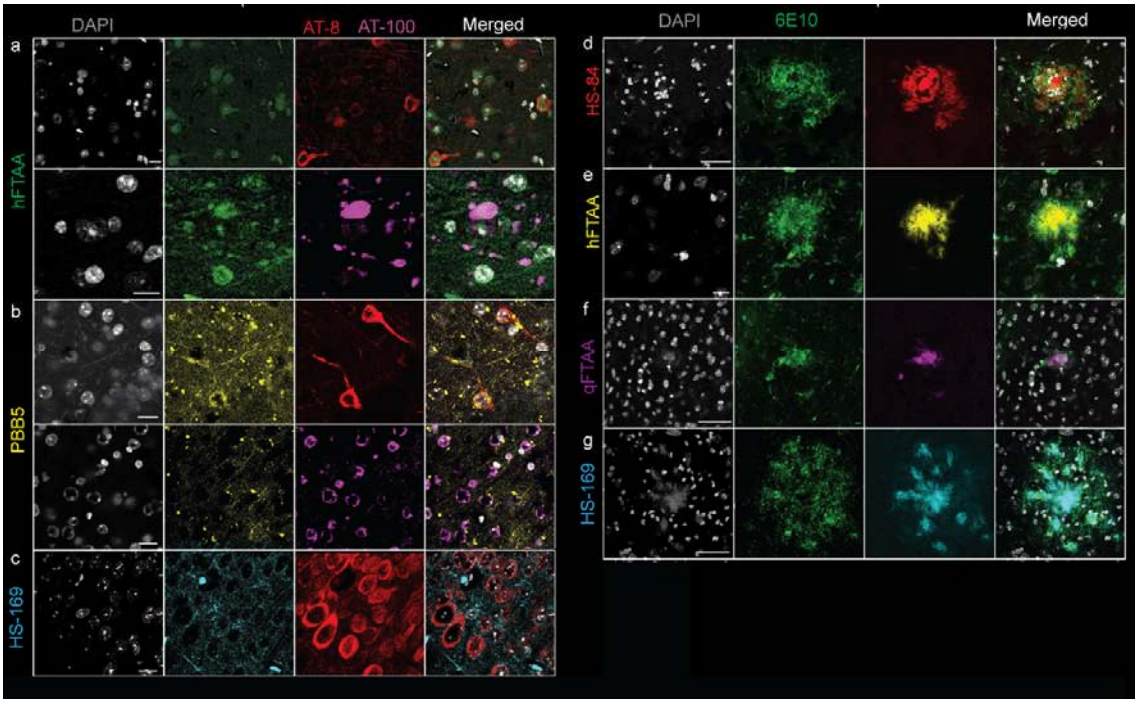

Fig. 6

Table 1. Information on brain tissue samples from patients with Parkinson's disease, nondemented control and animal models

Postmortem human brain sample								
No	**Sex**	**Age (y)**	**PM delay (h)**	**Braak tau**	**Amyloid-β**	**Braak LB**	**Diagnosis**	**Region**
1	M	61	7.5	1	O	6	PD	MO
2	M	65	4.8	0	O	6	PD	MO
3	M	83	5.3	1	O	6	PD	LC
4	F	69	8.5	1	-	0	NC	MO

Mouse brain sample				
Model	**Number**	**Sex**	**Age (m)**	**Region imaged**
αSyn PFF-injected mice	2	M	5.5	CeA, NAc, PPN, PAG, SNc
arcAβ mice	2	M/F	18	Ctx
pR5 mice	2	M/F	18	Hip
Nontransgenic littermate mice *	4	M/F	18	Ctx, Hip

Ctx, Cortex; CeA, central amygdala; LB, Lewy body; LC; MO, medulla oblongata; NAc, nucleus accumbens; NC, nondemented control; PD, Parkinson's disease; PM, postmortem; PPN, pedunculopontine nucleus; PAG, periaqueductal gray; SNc, substantia nigra pars compacta; * Two nontransgenic littermate mice for arcAβ and pR5 mice, respectively.

Table 2 Results of surface plasmon resonance measurements of αSyn fibrils and $A\beta_{42}$ fibrils, K18 and full-length tau fibrils

	Analyte	Surface	Surface density/ RU	k_{on}/$M^{-1}s^{-1}$	k_{off}/s^{-1}	K_D/ M	RU(max)	Chi^2
αSyn	HS-169	CMD200M	2940	2.88E+05	2.54E-03	8.8E-09	16.3	0.60
				1.45E+05	4.18E-02	2.89E-7	45.4	
	HS-84	CMD200M	3400	1.161E+04	5.45E-06	4.78E-10	22.5	0.59
				1.115E+06	6.02E-02	5.40E-08	42.2	
	h-FTAA	CMD200M	3400	1.62E+05	2.86E-03	1.77E-08	2.8	0.05
				1.11E+05	5.82E-02	5.23E-07	19.3	
	q-FTAA	CM5	2940	9.07E+05	1.52E-02	1.67E-07	26.7	0.99
				1.53E+03	7.05E-04	4.61E-07	60.9	
	MB	CMD200M	3400	4.72E+05	8.34E-01	1.77E-06	39.0	0.06
				4.57E+02	1.71E-02	3.75E-05	107.0	
K18 tau	HS-84	CMD200M	8280	4.89E+03	2.21E-03	4.52E-07	35.3	0.07
				3.59E+06	6.33E+0	1.76E-06	33.4	
	q-FTAA	CMD200M	8280	4.89E+02	3.14E-03	6.419E-06	47.9	0.16
				2.798E+03	5.85E-02	2.092E-05	32.1	
	h-FTAA	HC1500M	9010	5.32E+01	1.49E-04	2.81E-06	5968	0.19
				2.70E+02	3.02E-02	1.12E-04	900	
FL tau	HS-169	ZC150D	2900	6.78E+01	1.64E-05	2.41E-07	2216	2.23
				1.12E+04	8.09E-03	7.23E-07	67.6	
	Lan	ZC150D	2900	1.15E+02	1.74E-04	1.51E-06	2682	0.09
				5.03E+03	4.26E-02	8.47E-06	93.6	
$A\beta_{42}$	HS-169	ZC150D	1770	1.20E+02	1.67E-05	1.39E-07	641	0.49
				5.79E+02	1.05E-02	1.82E-05	367.3	
	Lan	ZC150D	1770	9.47E+02	1.63E-04	1.72E-07	383	0.07
				3.49E+03	3.81E-02	1.09E-05	98.9	

k_a / $M^{-1}s^{-1}$: Rate constants of association; k_d / s^{-1}: Rate constants of dissociation; K_D/ M the dissociation constant. Calculation using a sum of 2 exponentials kinetic model; RU (max) is response units (intensity) at the steady state; FL: full-length; Lan: lansoprazole; MB: methylene blue;

Supplemental Material

SFig 1. Chemical structures of the ligands and compounds

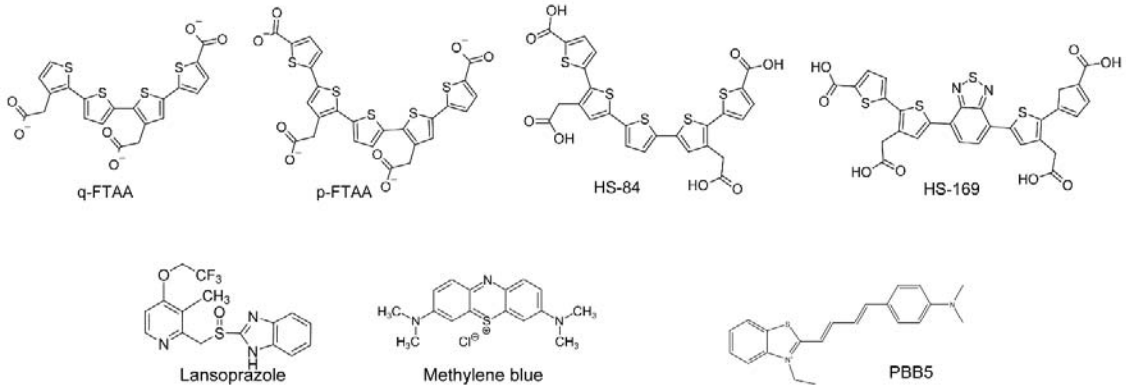

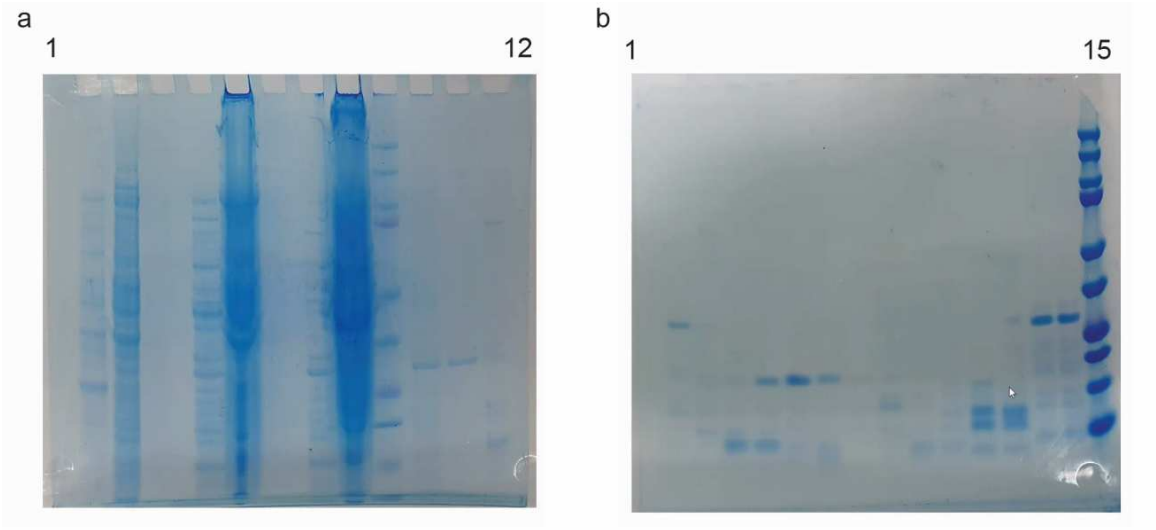

SFig 2. Confirmation of αSYN and K18 tau (**a**) αSYN purification (bands 1-12). After each step, an aliquot was taken, and ultimately, the identity was verified by sodium dodecyl sulfate–polyacrylamide gel electrophoresis (SDS–PAGE). The identity of αSYN was confirmed by a visible band at approximately 14 kDa (in band 12). From bands 1-12 (left to right): 1) *E. coli* uninduced (before adding IPTG), 2) *E. coli* induced, 3) empty, 4) osmotic shock (OS) supernatant (Sup.), 5) OS pellet, 6) empty, 7) heat shock (HS) supernatant, 8) HS pellet, 9) Bio-Rad Precision Plus Protein Dual Color Standards, 10) ammonium sulfate (AS) precipitation 35% supernatant, 11) AS 55% supernatant, 12) AS 55% pellet. (**b**) tau purification (bands 1-15). After centrifugation of the cell debris, the supernatant was recovered, and column chromatography with a phosphocellulose column was performed. Twelve elution fractions of the chromatography were obtained and verified by SDS–PAGE (bands 1-12, left to right). The three fractions with the highest Tau concentrations (fractions 4, 5, and 6) were selected for subsequent dialysis and lyophilization. Bands 13-15 were the solution before chromatography, the flow-through, and the reference band (Bio-Rad Precision Plus Protein Dual Color Standards).

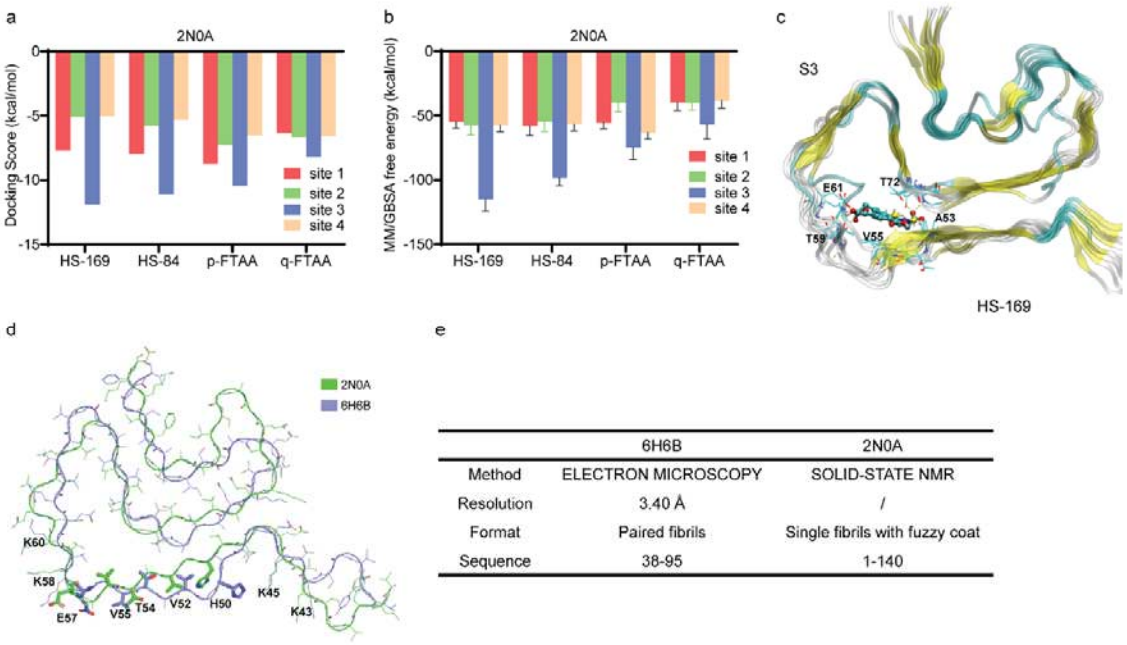

	6H6B	2N0A
Method	ELECTRON MICROSCOPY	SOLID-STATE NMR
Resolution	3.40 Å	/
Format	Paired fibrils	Single fibrils with fuzzy coat
Sequence	38-95	1-140

SFig 3. **In silico modelling of the binding sites of HS-169, HS-84, h-FTAA, p-FTAA and q-FTAA on the 2N0A alpha-synuclein structure.** (**a, b**) Docking and MM/GBSA calculation of free energy indicating that site 3 is preferred by HS-169, HS-84, h-FTAA, p-FTAA and q-FTAA on the 2N0A alpha-synuclein structure. (**c**) Zoomed-in view of HS-169 binding to site 3. (**d, e**) Difference between the 2N0A and 6H6B structures.